



Susceptibility of Microseismic Triggering to Small Sinusoidal Stress Perturbations at the Laboratory Scale

Martin Colledge, Jérôme Aubry, Kristel Chanard, François Pétrélis, Clara Duverger, Laurent Bollinger, Alexandre Schubnel

► To cite this version:

Martin Colledge, Jérôme Aubry, Kristel Chanard, François Pétrélis, Clara Duverger, et al.. Susceptibility of Microseismic Triggering to Small Sinusoidal Stress Perturbations at the Laboratory Scale. Journal of Geophysical Research : Solid Earth, 2023, 128 (4), 10.1029/2022JB025583 . hal-04093180

HAL Id: hal-04093180

<https://hal.science/hal-04093180>

Submitted on 11 May 2023

HAL is a multi-disciplinary open access archive for the deposit and dissemination of scientific research documents, whether they are published or not. The documents may come from teaching and research institutions in France or abroad, or from public or private research centers.

L'archive ouverte pluridisciplinaire **HAL**, est destinée au dépôt et à la diffusion de documents scientifiques de niveau recherche, publiés ou non, émanant des établissements d'enseignement et de recherche français ou étrangers, des laboratoires publics ou privés.



Distributed under a Creative Commons Attribution 4.0 International License

JGR Solid Earth

RESEARCH ARTICLE

10.1029/2022JB025583

Key Points:

- The response amplitude of acoustic emissions (AEs) is proportional to the amplitude of the stress oscillations
- The response amplitude of AEs increases with both the oscillation period and background loading rate
- The Gutenberg-Richter b -value is modulated by stress oscillations

Supporting Information:

Supporting Information may be found in the online version of this article.

Correspondence to:

M. Colledge,
colledge@geologie.ens.fr

Citation:

Colledge, M., Aubry, J., Chanard, K., Pétrelis, F., Duverger, C., Bollinger, L., & Schubnel, A. (2023). Susceptibility of microseismic triggering to small sinusoidal stress perturbations at the laboratory scale. *Journal of Geophysical Research: Solid Earth*, 128, e2022JB025583. <https://doi.org/10.1029/2022JB025583>

Received 8 SEP 2022

Accepted 11 APR 2023

Author Contributions:

Conceptualization: Martin Colledge, Kristel Chanard, François Pétrelis, Alexandre Schubnel

Data curation: Martin Colledge, Jérôme Aubry

Formal analysis: Martin Colledge, Kristel Chanard, François Pétrelis, Alexandre Schubnel

Funding acquisition: Laurent Bollinger, Alexandre Schubnel

Investigation: Martin Colledge, Jérôme Aubry, Kristel Chanard, Clara Duverger, Laurent Bollinger, Alexandre Schubnel

Methodology: Martin Colledge, Jérôme Aubry, Alexandre Schubnel

Project Administration: Laurent Bollinger, Alexandre Schubnel

© 2023. The Authors.

This is an open access article under the terms of the [Creative Commons Attribution License](https://creativecommons.org/licenses/by/4.0/), which permits use, distribution and reproduction in any medium, provided the original work is properly cited.

Susceptibility of Microseismic Triggering to Small Sinusoidal Stress Perturbations at the Laboratory Scale

Martin Colledge^{1,2} , Jérôme Aubry^{1,2} , Kristel Chanard³, François Pétrelis⁴, Clara Duverger² , Laurent Bollinger² , and Alexandre Schubnel¹ 

¹Laboratoire de Géologie, École Normale Supérieure, PSL University, CNRS, Paris, France, ²CEA, DAM, DIF, Arpajon, France, ³Université Paris-Cité, Institut de physique du globe de Paris, CNRS, IGN, Paris, France, ⁴Laboratoire de Physique de l'École Normale Supérieure, ENS, PSL University, CNRS, Sorbonne Université, Université Paris-Diderot - Paris, Paris, France

Abstract Small transient stress perturbations are prone to trigger (micro)seismicity. In the Earth's crust, these stress perturbations can be caused by various sources such as the passage of seismic waves, forcing by tides, or hydrological seasonal loads. A better understanding of the dynamic of earthquake triggering by stress perturbations is essential to improve our understanding of earthquake physics and our consideration of seismic hazard. Here, we study an experimental sandstone-gouge-filled fault system undergoing combined far field loading and periodic stress perturbations (of variable amplitude and frequency) at crustal pressure conditions. Microseismicity—in the form of acoustic emissions (AEs)—strains, and stresses, are continuously recorded in order to study the response of microseismicity as a function of loading rate, amplitude, and frequency of a periodic stress perturbation. The observed AE distributions do not follow the predictions of either a Coulomb failure model, taking into account both constant loading and oscillation-induced strain rates, or a rate and state model. A susceptibility of the system's AE response to the amplitude of the confinement pressure perturbation is estimated, which highlights a linear relation between confinement pressure amplitude and the AE response amplitude, observations which agree with recent higher frequency experimental results on dynamic triggering. The magnitude-frequency distribution of AEs is also computed. The Gutenberg-Richter b -value oscillates with stress oscillations. Our experiments may help complement our understanding of the influence of low inertia stress phenomena on the distribution of seismicity, such as observations of dynamic triggering and seismicity modulation by tides or hydrological loading.

Plain Language Summary Stresses exerted on faults are constantly subjected to fluctuations related to the periodicity of external forces applied to the Earth's crust, for example, tidal forces, or seasonal variations in water loads. These stress variations have been linked to time periods when earthquakes are more likely to occur in some specific contexts, but the precise mechanisms at play are not fully understood. Experimental work is here conducted to examine the influence of several key parameters, namely oscillation period and amplitude and background tectonic velocity, on the occurrence of laboratory-scale microseismicity. Microseismicity periodicity is proportional to the stress oscillation amplitude, and both short oscillation period and low tectonic velocity cause microseismicity to correlate less with the stress oscillations, possibly explaining why short-period tides do not correlate well with seismicity whereas long-period seasonal variations in stress have been shown to correlate with seismicity. The ratio between small and large events also appears to correlate with the stress oscillation, suggesting that stress oscillations might create conditions during which large events are more likely to occur.

1. Introduction

Earthquakes originate from the sudden release of elastic stresses on faults. These stresses are primarily built-up by tectonic processes over long periods of time. However, transient and oscillatory stress phenomena such as tidal, hydrological, or dynamic loading due to seismic wave propagation also contribute to stressing faults. The existence of these stresses leads to the question of their role on earthquake nucleation and triggering. This question has historically been debated (e.g., Davison, 1938; Hartzell & Heaton, 1989; Heaton, 1982; Klein, 1976; Schuster, 1897), with numerous studies claiming either the existence or the absence of evidence of seismic periodicities at timescales corresponding to the invoked phenomena, with statistical limitations due to catalog sizes, selection, and biases keeping the question from being settled. Recent rigorous studies have highlighted the

Resources: Martin Colledge, Alexandre Schubnel

Software: Martin Colledge

Supervision: Jérôme Aubry, Kristel Chanard, François Pétrélis, Clara Duverger, Laurent Bollinger, Alexandre Schubnel

Validation: Martin Colledge

Visualization: Martin Colledge

Writing – original draft: Martin Colledge

Writing – review & editing: Martin Colledge, Jérôme Aubry, Kristel Chanard, François Pétrélis, Clara Duverger, Laurent Bollinger, Alexandre Schubnel

existence of periodic variations in seismicity rates in various tectonic settings, such as annual variations of seismicity in continental collision zones such as the Himalayas (Ader & Avouac, 2013; Bettinelli et al., 2008; Bollinger et al., 2007), in faults located near subduction zones as in Taiwan (Hsu et al., 2021) and Japan (Heki, 2003), in non-deforming intraplate regions such as the New-Madrid Seismic Zone (Craig et al., 2017), and even in the case of deep-focus earthquakes (Zhan & Shearer, 2015). Observations of tidal variations of seismicity have also been made in various seismotectonic settings, including along shallow thrust faults (Cochran et al., 2004), as well as in seismicity associated with geothermal (Wang et al., 2022) and submarine volcanic activity (Tolstoy et al., 2002). Tidal forces have also been linked to the triggering of tectonic tremors (e.g., Chen et al., 2018; Ide & Tanaka, 2014; Rubinstein et al., 2008) and slow slips (Hawthorne & Rubin, 2010). Moreover, the dynamic triggering of earthquakes by transient oscillatory stress changes caused by seismic waves has largely been accepted (e.g., Anderson et al., 1994; Brodsky & van der Elst, 2014; Hill et al., 1993).

All these observations are difficult to interpret due to differences between studies, with significant changes in tectonic contexts, fault geometry, and oscillation frequency and amplitude. Theoretical and numerical studies have attempted to unify all these observations, invoking nucleation times relative to the period of the stress oscillations as one of the factors differentiating a stress controlled regime from a stressing rate controlled regime (Ader & Avouac, 2013; Beeler & Lockner, 2003; Dublanchet, 2022; Heimisson & Avouac, 2020; Perfettini et al., 2001), or suggesting magnitude-dependent and oscillation-geometry-dependent modulation (Pétrélis et al., 2021). Experimental studies focused on the links between stress oscillations and seismicity have investigated the increased synchronization of the temporal distribution of AEs with periodic stress oscillations prior to macroscopic failure (Chanard et al., 2019; Noël, Pimienta, & Violay, 2019) and either the triggering or the induced clock-advance of stick-slips (Bartlow et al., 2012; Chelidze et al., 2010; P. A. Johnson & Jia, 2005; P. A. Johnson et al., 2008; Lockner & Beeler, 1999; Savage & Marone, 2007, 2008).

To the best of our knowledge, no study has investigated the influence of stress oscillation parameters on AEs distributions in granular shear experiments, such that observations of seismicity modulation in different natural tectonic contexts lack sufficient experimental references. Furthering our understanding of the role of small periodic stress changes on earthquake triggering could have implications for earthquake hazard assessment. This has been highlighted by observations of magnitude-frequency distribution (*b*-value) variations due to tides (Ide et al., 2016) as well as by observations of gradually increased correlation of seismicity with tides before large megathrust earthquakes, which could signify that seismic response of faults close to failure grow more susceptible to stress variations (Tanaka, 2010, 2012). These latter observations have, however, been called into question for their statistical significance (Wang & Shearer, 2015) although experimental results support the validity of the theory on which they are based (Chanard et al., 2019; Noël, Pimienta, & Violay, 2019). These elements act as further motivation to experimentally investigate the question.

In this study, we perform shearing experiments on a granular fault gouge analog at different strain rates, in order to mimic different tectonic loading rates. Confinement pressure oscillations are applied and AEs within the gouge are monitored. The magnitude and phase of these AEs is then computed and analyzed. We start by presenting our experimental set-up and the range of parameters explored within our study. We then present experimental results in the form of stress and friction evolution with slip, and temporal distribution variations and magnitude properties of AEs. The modulation of the temporal distribution of the AEs is then quantified, and both the influence of the loading and oscillation parameters, and the variations of magnitude-frequency distributions with the stress oscillations are discussed. Finally, we consider an upscaled interpretation of our results and address their implications for seismology.

2. Materials and Methods

2.1. Material and Sample Preparation

Experiments are performed on matching aluminum cylindrical guide blocks (“saw-cuts”) featuring corrugated planar surfaces oriented 30° from the axial direction (Figure 1a and Figure S1 in Supporting Information S1). In order to mimic naturally occurring gouge-filled faults, we place 20 g of gouge—the equivalent of a roughly 5 mm thick layer—between the saw-cuts, which we enclose with aluminum tape. The gouge is generated by crushing pieces of Fontainebleau sandstone—a well-studied sandstone known for its purity and its homogeneous composition of quartz grains of characteristic size 250 μm (Bourbie & Zinszner, 1985)—down to a fine polydisperse

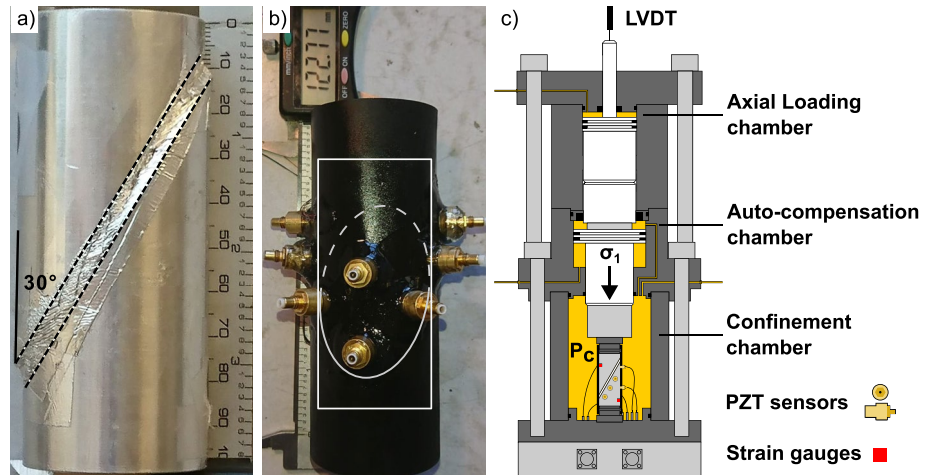


Figure 1. Sample setup. Post-experiment saw-cuts with (a) gouge cased in aluminum tape; (b) neoprene jacket and piezoceramic transducers (PZT) used as acoustic sensors. The ellipse indicates the fault location. (c) Schematic of the triaxial apparatus and sample—modified from Fortin et al. (2007).

gouge, with the largest grain size matching the characteristic grain size (Figure S2 in Supporting Information S1). The experiment is designed with an artificial fault with gouge to produce enough AEs for statistical significance of the AEs catalog analysis, a criterion not met by experiments using bare rocks as fault analogs. The use of gouge to investigate microseismicity experimentally is not a novel approach (e.g., Bolton et al., 2019, 2022; P. A. Johnson et al., 2013; Mair et al., 2007).

2.2. Sample Instrumentation

The sample is equipped with both acoustic sensors and strain gauges to monitor AEs and deformation during experiments. Double component strain gauges (FCB-2-11, 120 Ω by Tokyo Sokki Kenkyujo Co., Ltd, Japan) are glued on each saw-cut to measure strain in both axial and radial directions. The saw-cuts are then inserted into a neoprene jacket. Eight acoustic transducers, consisting of a piezoelectric (PZT) crystal (PI CERAMIC PI255, 5 mm diameter, 2 mm thickness, 1 MHz central frequency) sensitive to P waves (normal to the sample-sensor surface) are encased within brass holders. These are glued directly onto the lower guide block surface, in a wide formation depicted in Figure 1b and Figure S3 in Supporting Information S1. More information on the sensors can be found in Brantut et al. (2011). The array is designed to achieve homogeneous coverage, with sensors as close as possible to the gouge layer to detect the smallest possible AEs. Finally, to ensure proper sealing from the pressurized oil present in the confining chamber, a bi-component epoxy resin is applied on the neoprene jacket around the holes punctured within the jacket for strain-gauges and acoustic transducers inserts.

2.3. Apparatus

The sample is inserted into a triaxial apparatus at the École Normale Supérieure in Paris. One important feature of this experimental system is the presence of an auto-compensated confinement chamber, that is, a chamber which counterbalances the confining pressure exerted on the piston. More details can be found in Schubnel et al. (2005). The auto-compensation process depends on both the main confinement chamber and the auto-compensation chamber being at the same pressure. Therefore, changes in the confining pressure need to be gradual in order for the pressures in the main confinement chamber and the auto-compensation chamber to equilibrate.

Piston displacement, applied axial stress (σ_1), confining pressure (P_c), as well as differential stress ($\Delta\sigma = \sigma_1 - P_c$), radial and axial strains measured by strain gauges are recorded with a sampling rate of 10 Hz with a digital encoder (HBM MGC Plus). Resolution on acquired stresses is $\sim 10^{-3}$ MPa and 10^{-6} on strains.

From these measurements, the shear stress τ and normal stress σ_N applied in the oblique direction of the gouge layer can respectively be derived as follows:

$$\tau = \frac{\Delta\sigma}{2} \sin(2\alpha) \quad (1)$$

Table 1
Experimental Velocity Segments Detail

Segment order	Injection rate (cc/hr)	Displacement d_p (mm)	Average slip velocity \bar{V} ($\mu\text{m/s}$) ^a	Segment duration t_{segment} (hr:min)
1	50	1.5	1.2 ± 0.1	00:20
2	10	0.5	0.32 ± 0.05	00:30
3	2	0.5	0.069 ± 0.004	02:10
4	0.4	1.0	0.014 ± 0.0003	22:10
5	2	0.5	0.074 ± 0.003	02:10
6	10	0.5	0.37 ± 0.03	00:30
7a ^b	50	0.5	1.9	00:06
7b ^c	50	1.0	1.9 ± 0.1	00:12

^aThe difference in average slip velocity \bar{V} for segments of identical injection rates is due to the elastic response of the saw-cuts and apparatus, which accommodates part of the displacement of the piston, as well as due to the gouge sample maturing throughout the experiment. ^bSegment 7a is the last segment of the control experiment. ^cSegment 7b is the last segment of all oscillation experiments.

$$\sigma_N = \frac{\Delta\sigma}{2}(1 + \cos(2\alpha)) + P_c \quad (2)$$

where $\Delta\sigma$ is the differential stress, α is the angle between the axial direction and the normal to the gouge plane (here $\alpha = 60^\circ$) and P_c is the confining pressure.

The piston displacement is measured with a Linear Variable Differential Transformer (LVDT) placed atop the piston with a $\sim 0.1 \mu\text{m}$ resolution. Throughout the experiments, the piston and the aluminum saw-cuts undergo elastic shortening. The measure given by the LVDT as the piston advances therefore does not correspond to the actual slip occurring within the gouge. Slip δ is determined by correcting for the elastic contributions of both the machine and the saw-cuts, as follows:

$$\delta = \frac{\left(d_p - kF - \frac{\Delta\sigma}{E_{al}}L\right)}{\cos(\pi - \alpha)} \quad (3)$$

where d_p is the raw displacement measured on the top of the piston by the LVDT, k (m/N) is the machine compliance, F is the applied load (equal to $F = \Delta\sigma\pi r^2$, with r the sample radius), and L and E_{al} are the aluminum sample length and Young's modulus respectively.

2.4. Experimental Procedure

Once sealed inside the confinement chamber, the confining pressure exerted on the sample is raised and kept overnight at 90 MPa in order for the gouge to undergo compaction and comminution. During this stage, several thousands of acoustic emissions (AEs) are detected, showcasing the effective compaction of the gouge via grain crushing and grain contact rearrangement. The confining pressure is then lowered to 50 MPa—corresponding to depths of approximately 2 km under typical lithostatic pressure conditions—for the rest of the duration of the experiment.

The sample is then loaded axially, the piston displacement being hydraulically servo-controlled via a high-pressure syringe pump. Displacement rate is controlled as a proxy by oil injection rate into the piston upper pressure chamber. A high injection rate segment of 50 cc/hr (corresponding to a piston velocity V_p of roughly $1 \mu\text{m/s}$) is first applied for a displacement of 1.5 mm, to elastically load the system, compact the gouge further and approach a frictional steady-state. We then perform constant injection rate segments, first lowering the velocity three times from around $1 \mu\text{m/s}$ down to a minimum of approximately 10 nm/s, then raising the velocity by repeating the use of the previous velocity segments in reverse order. A displacement of 0.5 mm is allowed at each velocity segment, and the segment duration t_{segment} is therefore determined by the loading velocity. For each segment, the slip velocity V is also computed (see Table 1). The slowest segment, which lasts approximately a full day, is not repeated twice but is lengthened to ensure the measured displacement during the segment is twice that of faster segments. These velocity segments are undertaken to characterize the frictional stability behavior of the gouge at these strain rates, as well as to investigate the influence of loading rate on the temporal distribution of AEs.

In total, six experiments are conducted following this axial loading procedure. A first experiment is conducted by simply following the loading procedure and is used as the control experiment. During the remaining five experiments, oscillations are introduced in the confining pressure, as detailed in Table 2. The investigated oscillation amplitudes correspond to 5%, 1%, and 0.2% of the imposed confining pressure depending on the experiment.

Confining pressure oscillations are performed via a second servo-controlled hydraulic syringe pump. The oscillations are quasi-sinusoidal (by setting separately the amplitude, rate, acceleration, and period of the pressure oscillation). Three important experimental limitations need to be pointed out:

Table 2
Imposed Oscillation Parameters and Total Acoustic Emission Count in Experiments

Experiment #	Stress oscillation amplitude, ΔP_c (MPa)	Stress oscillation period, T (s)	Acoustic emissions
0 (Control)	N.A.	N.A.	15,651
1	0.5	100 ± 2	18,152
2	0.1	100 ± 2	15,503
3	2.5	100 ± 2	6,358
4	0.5	20 ± 0.4	19,821
5	0.5	500 ± 10	8,742

1. The confining pressure oscillations generate shear stress oscillations, albeit smaller, due to elastic couplings and to the geometry of the experimental setup.
2. It is impossible with our system to perform confining pressure oscillations, while also maintaining the confining pressure average constant. In consequence, the experiments with oscillations are performed under “constant pressurized volume” conditions, which lead, because of oil leakage, to a small pressure drop at the beginning of our experiment, followed by slow variations in the average confining pressure over the course of the experiments. These slow pressure changes are not significant at the timescale of the imposed oscillations.
3. The period of oscillation is limited by a lower bound due to the presence of an auto-compensation chamber, which precludes the investigation of very short periods. An upper bound to the oscillation period also exists with our experimental procedure, as we wish to observe multiple oscillation periods within each velocity segment. The oscillation period must therefore be shorter than the duration of the shortest velocity segment.

Finally, the apparatus used to impose the stress oscillations does not produce oscillations of exactly the specified period and can deviate from the imposed value by up to 2%. To improve the determination of the oscillation period, a Fourier Transform is applied to the confining pressure measurements. A Gaussian fit is then applied to the power spectrum in a frequency range surrounding the imposed period to determine the true oscillation period with improved precision (Gasior & Gonzalez, 2004). When the confining pressure measurements display discontinuities due to either erroneous values that require removing (Figure S4 in Supporting Information S1) or software restarts, the overall period is determined by taking an average of the thus derived periods weighted by the length of each segment. Calculations of the period over these segments give period estimates that are in good agreement with one another.

2.5. Rate and State Parameters Calculation

As velocity changes are applied during our experimental procedure, the constitutive rate and state parameters of our sample can be retrieved. Indeed, according to the rate and state friction model (Dieterich, 1981), the friction coefficient is defined as follows:

$$\mu = \frac{\tau}{\sigma_N} \quad (4)$$

is dependent on both the rate of displacement and a state variable θ , such that during a velocity change from V_o to V the friction coefficient, is defined as follows:

$$\mu(\theta, V) = \mu_o + A \ln\left(\frac{V}{V_o}\right) + B \ln\left(\frac{V_o \theta}{D_c}\right) \quad (5)$$

where μ_o is the initial friction coefficient measured at V_o , A , and B are constitutive parameters and D_c is the macroscopic critical slip distance over which the friction coefficient reaches its new steady-state value. The state variable θ is commonly defined with two empirical formulations (Ampuero & Rubin, 2008; Ruina, 1983), known as the slip law:

$$\dot{\theta} = -\frac{V\theta}{D_c} \ln\left(\frac{V\theta}{D_c}\right) \quad (6)$$

and the aging law:

$$\dot{\theta} = 1 - \frac{V\theta}{D_c} \quad (7)$$

The rate and state parameters A , B , and D_c are determined for the control experiment using the RSFIT3000 Matlab GUI (Skarbek & Savage, 2019).

2.6. Acoustic Data Methodology

2.6.1. AEs Detection and Processing

AEs are detected in triggering mode, that is, by applying a voltage-threshold trigger logic, requiring at least 3 of the 8 acoustic sensors to reach a specified voltage (typically 100 mV, once amplified at 45 dB – x150) within a given time window (typically 50 μ s) for waveforms to be recorded. Waveforms of 8,192 data points are recorded at 14 bit, with a 10 MHz sampling rate using an eight channel digital oscilloscope. Recording, storage,

management, and basic data processing are performed using a licensed software (Insite, Applied Seismology Consulting Ltd.). The threshold trigger criteria are set through trial and error to be just above the background noise level of the acoustic monitoring. The threshold trigger criteria are also set so that the AE productivity rate remains below the maximum triggering rate capability (~ 50 AE/s) of the hardware throughout the experiment, at least after the first velocity segment.

Waveforms are first filtered with a two-pass low-pass filter of cut-off frequency 2 MHz to remove noise and better detect AEs. An STA/LTA auto-picking procedure (Trnkoczy, 2009) is manually tuned to each sensor in each experiment after suppressing low signal-to-noise records to precisely determine the arrival time of the P waves resulting from the AEs. In our catalogs, timing of AEs correspond to the P -picks arrival times as the travel times within the sample (less than 10 μ s) are negligible compared to the imposed stress oscillations periods. Using the average Root Mean Square (RMS) of the AE waveforms, relative magnitudes M_r are calculated following Rivière et al. (2018) as follows:

$$M_r = \log_{10} \left(\frac{\sum_1^n RMS}{n} \right) \quad (8)$$

with n the number of working AE sensors. Absolute magnitudes can also be determined by fitting, after careful sensor calibration (Marty, 2020), the average displacement spectra for each AE using the Ω^{-2} law (Madariaga, 1976).

2.6.2. Coherent Averaging of the AE Temporal Distribution

To determine whether discrete AEs are correlated with the applied stress oscillations over the many periods present in each velocity segment, a coherent averaging distribution of AEs is calculated by considering where each AE lies relative to the phase of the stress oscillation:

$$\phi \equiv \left(2\pi \frac{t - t_0}{T} \right) \mod 2\pi \quad (9)$$

where ϕ is the phase at which the AE occurs within the oscillation, t is the time at which the AE occurs, t_0 is the reference time of the oscillations defined as the time of a stress oscillation maximum, and T is the stress oscillation period. This average distribution is a useful quantification of the average temporal distribution of AEs.

2.6.3. Magnitude Frequency Distribution

The magnitude distribution of AEs in laboratory experiments has repeatedly (e.g., Lockner, 1993; Marty, 2020; Meredith et al., 1990; Mogi, 1962; Scholz, 1968) been shown to follow the same distribution as earthquakes, that is, the Gutenberg-Richter (GR) law:

$$N(M) = 10^{a-bM} \quad (10)$$

where N is the number of events of magnitude greater than M that occur, a and b being constants. The b -value of the GR-law describes the ratio of occurrence of large to small magnitude emissions and corresponds to the slope of the magnitude distribution above a certain cut-off magnitude M_c , called completeness magnitude, under which catalogs are viewed as incomplete. The b -value is calculated using both a least squares method and a maximum likelihood estimate (Aki, 1965), the latter being considered more accurate. Indeed, larger magnitude ranges are given less weight, thus accounting in some measure for the uncertainty linked to the small sample size of larger magnitude emissions.

3. Experimental Results

3.1. Control Experiment

3.1.1. Mechanical Behavior

As axial loading is applied to the sample, the normal and shear stresses applied on the fault increase (Figure 2). The sample accommodates a small amount of stress through elastic deformation before slip initiates. After the initiation of slip, the stresses continue increasing and tend toward an asymptotic steady-state behavior, corresponding to a friction coefficient of 0.7 (Figure 3a). This value is comparable to those generally observed in the literature for quartz-based gouges (e.g., Bedford et al., 2022; Leeman et al., 2016; Marone et al., 1990; Marone & Scholz, 1989; Samuelson et al., 2009).

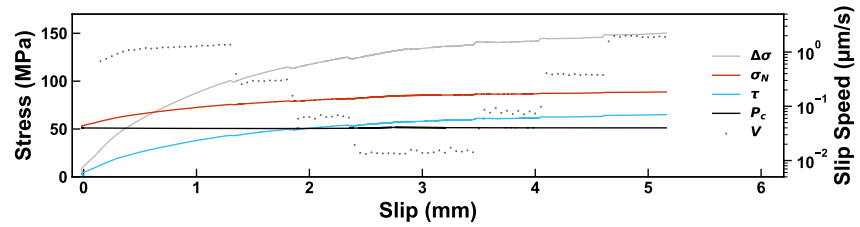


Figure 2. Stresses evolution during the control experiment. As the piston must first overcome the static friction threshold to advance, the differential stress first increases without any recorded piston displacement. Slip is therefore overcorrected before the onset of slip, with negative slip values appearing at the onset of the experiment.

3.1.2. Rate and State Parameters

Both the slip law and the aging law of the state variable are used for the calculation of the rate and state parameters, with very similar values being obtained with both laws. The fit of the friction coefficient evolution and rate and state parameters presented in Figures 3b and 3c correspond to the slip law. $A - B$ decreases slightly during the experiment from an initial value of roughly $4e-3$ down to a value of roughly $2.5e-3$, and D_c increases slightly from roughly 60 to 80 μm . Such changes in frictional properties with shear displacements are common in gouge experiments (e.g. Beeler et al., 1996; Dieterich, 1981).

Due to the increase in friction coefficient with slip, a detrending procedure is applied to the friction coefficient in order for the rate and state fitting to only consider the effect of the velocity change. This is done by fitting low order polynomials to the friction data and running RSFit3000 calculation on the fit residuals.

Due to our experimental geometry, the sliding surfaces are not orthogonal to the loading axes. As such, loading velocity changes induce both shear stress and normal stress changes, the latter inducing additional frictional changes due to the Linker-Dietrich effect (Linker & Dieterich, 1992). The rate and state parameters determined here therefore capture the effect of both the velocity change and the normal stress change. Still, the absence of macroscopic stick-slip in our experiments is the confirmation that the main conclusion of this calculation, that the gouge is velocity strengthening at the imposed velocities—that is, that $A - B > 0$ —holds ground (Marone, 1998).

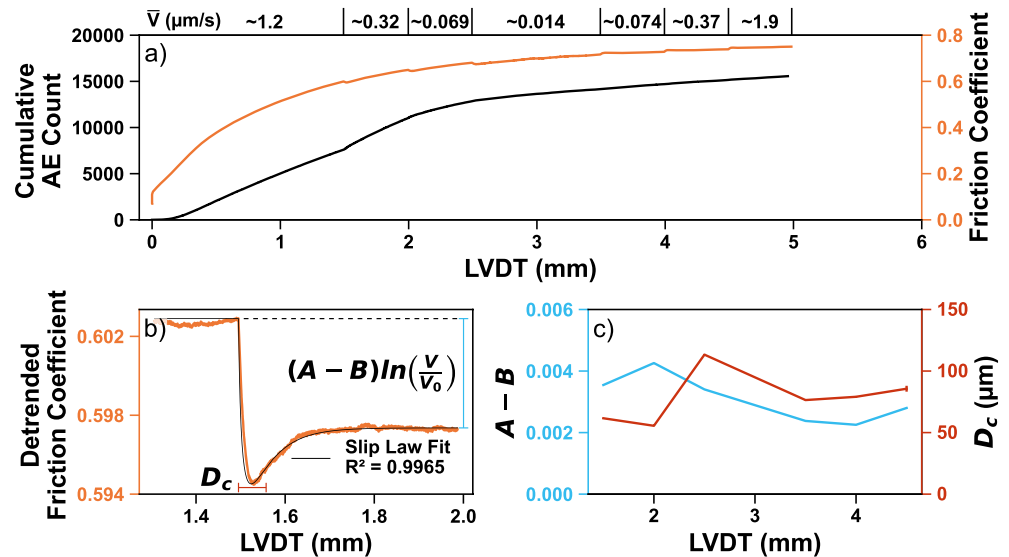


Figure 3. Control experiment frictional parameters. (a) Friction coefficient and cumulative acoustic emission count during the experiment. The last velocity segment is half as long as in oscillation experiments. (b) RSFit3000 fit of the first velocity change after removal of the friction coefficient long-term trend. The rate and state parameter $A - B$ corresponds to the non-transient change of friction coefficient caused by the velocity change. D_c is the macroscopic length scale of the friction coefficient transient state at a velocity change. All other fits are shown in Figure S7 in Supporting Information S1. (c) Rate and state $A - B$ and D_c parameters and associated two standard deviations determined by RSFit3000 as estimated from the control experiments at each velocity change.

The absence of stick-slip is convenient for the study of the temporal distribution of AEs. Indeed, the clustering of the AEs catalog into simple foreshock—mainshock—aftershock series is much reduced, and allows the presence of many smaller acoustic events, which lead to larger catalogs more suitable for statistical analysis. Whilst the gouge itself also undergoes strain, quantifying it precisely is not possible within our experiment. The gouge is therefore assumed to not undergo major changes in thickness after an initial compaction regime visible in the first few velocity segments of our experiment (Figure 3a), with both the friction coefficient and the AE rate reaching a plateau.

3.2. Oscillation Experiments

3.2.1. AE Rate and Mechanical Properties

All stress modulation experiments demonstrate the same evolution in AE rate and friction as the control experiment (Figure S6 in Supporting Information S1 and Figure 3), and exhibit similar numbers of AEs to the control experiment (Table 2). An initial compaction regime characterized by high AE rates and low friction coefficients progressively transitions into a stable regime with consistently low emission rates and high friction coefficients in the later velocity segments.

The imposed stress oscillations induce fluctuations in shear and normal stress (Figure 4 and Figure S5 in Supporting Information S1), AE-rate (Figure 5), friction coefficient (Figure S6 in Supporting Information S1), and slip velocity on the fault plane (Figure S9 in Supporting Information S1). The amplitude of the friction coefficient oscillations remains approximately constant at all velocities within an experiment (Figure S6 in Supporting Information S1). The amplitude of the shear stress and normal stress oscillations, however, are highly dependent on the slip velocity and on the imposed stress oscillation parameters (Figure S5 in Supporting Information S1). Most notably, the shear stress oscillations are of the highest amplitude for the highest average slip velocities.

3.2.2. AE Temporal Distribution Relative to the Stress Oscillation

As illustrated in Figure 5, AEs are not distributed uniformly over the stress oscillation but occur preferentially around specific phases, except for the lowest stress oscillation amplitude. This non-uniformity of the AE distributions is herein referred to as the modulation of the AE distribution. The influence of the oscillation amplitude on the distribution is greatly noted, the influence of the average slip velocity is also apparent. The higher the stress oscillation amplitude and the higher the average slip velocity, the more AEs are modulated. The influence of the period seems less significant.

3.2.3. AE Magnitudes

Absolute magnitudes range roughly between -9 and -7 (Figure 6) and do not vary significantly in distribution across experiments. Comparing absolute and relative magnitude estimates for each AE shows a good agreement between magnitudes sets, both scaling linearly at the first order (Figure 6a), thus verifying the validity and reliability of the absolute magnitudes. This is important as absolute magnitude could not be computed for all AEs due to numerical difficulties when fitting the Ω^{-2} law reliably on waveforms with poor signal-to-noise ratio. In the following, magnitude statistics are therefore computed using the RMS method (described in Section 2.6), and assigning to relative magnitudes the corresponding absolute magnitude obtained by calibration and the Ω^{-2} law fitting.

The b -values calculated in our experiments are relatively high (Figure 6b), with little variation being noted from one experiment to the other.

The maximum likelihood estimations consistently yield smaller values between 2.8 and 3.3 whilst the least squares fits range between 3 and 4.5. This larger spread of b -values produced by the least squares method is expected due to its reliance on large emissions, of which the amount is highly variable due to the stochastic nature of AEs. Though rarely found associated with natural background seismicity of which b -values typically fall around 1, high b -values have been observed in seismic swarms (Adhikari et al., 2021) as well as in the presence of fluids (Bachmann et al., 2012; Murru et al., 1999). Such high b -values estimates could also in part be due to the relatively small dynamic range between the completeness magnitude and the maximum magnitude, which can cause overestimation of b -values, as discussed by Geffers et al. (2022) and Marzocchi et al. (2020).

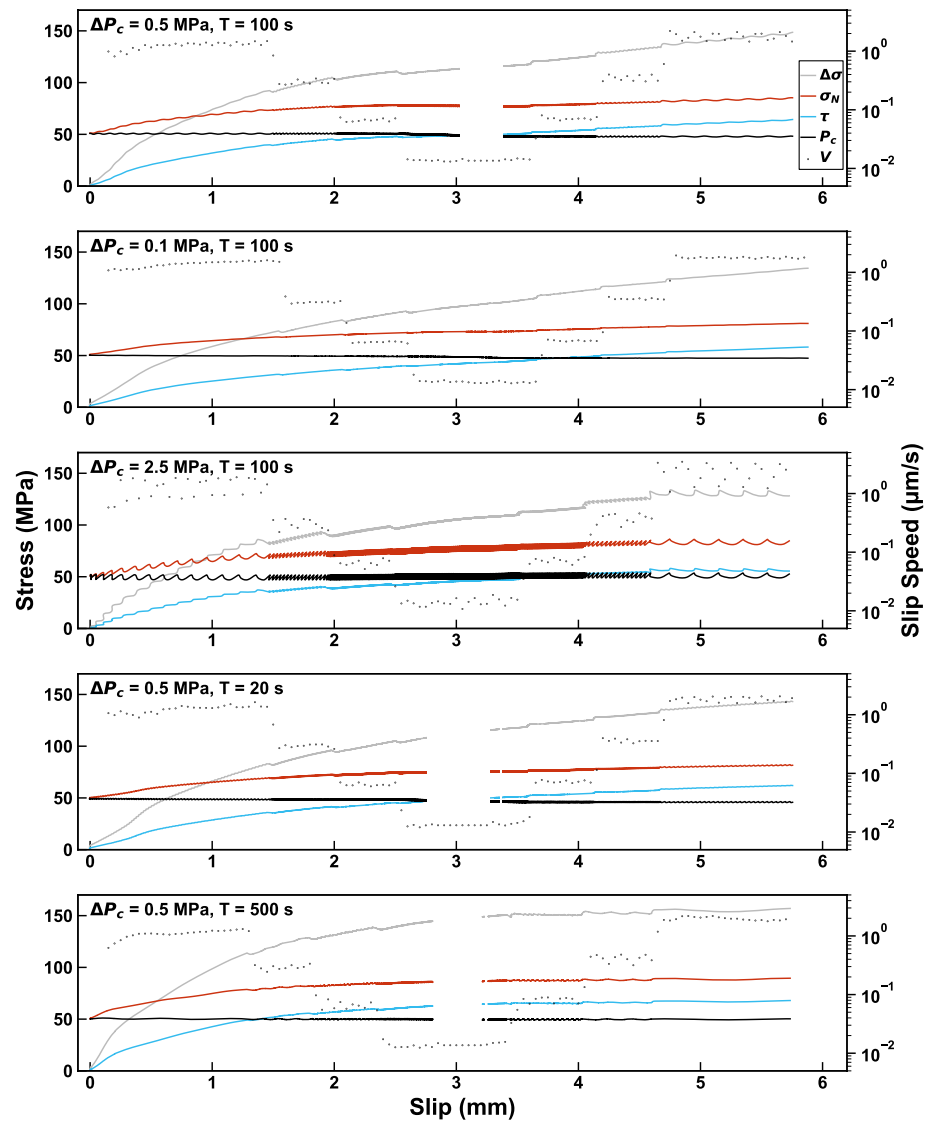


Figure 4. Stresses evolution during oscillation experiments. P_c oscillations impose oscillation on the differential, normal, and shear stresses. Holes in the time series correspond to periods of either erroneous or missing data (Figure S4 in Supporting Information S1).

4. Discussion

4.1. Coulomb Failure Model

When considering the effect of periodic stress on seismicity modulation and triggering, Coulomb failure stress is often invoked (e.g., C. W. Johnson et al., 2017; Scholz et al., 2019). Assuming a stable mechanical regime and according to Beeler and Lockner (2003) and Knopoff (1964), at oscillation periods larger than the nucleation time of microseismicity, a nucleation model based on Mohr-Coulomb failure should explain the distribution of the nucleation of microseismicity. In this theoretical framework, an AE occurs whenever the nucleation threshold is locally reached within the stress field. At oscillation periods smaller than the nucleation time, however, microseismicity should show reduced correlation with the oscillations.

Let us here consider the case of the Coulomb failure model, where strain is dissipated solely by nucleation of AEs. Due to the stochastic nature of AE nucleation, to the local unloading of stress by AEs, and to local geometric heterogeneities within the gouge, the stress field in the gouge is not homogeneous. We here assume a randomly

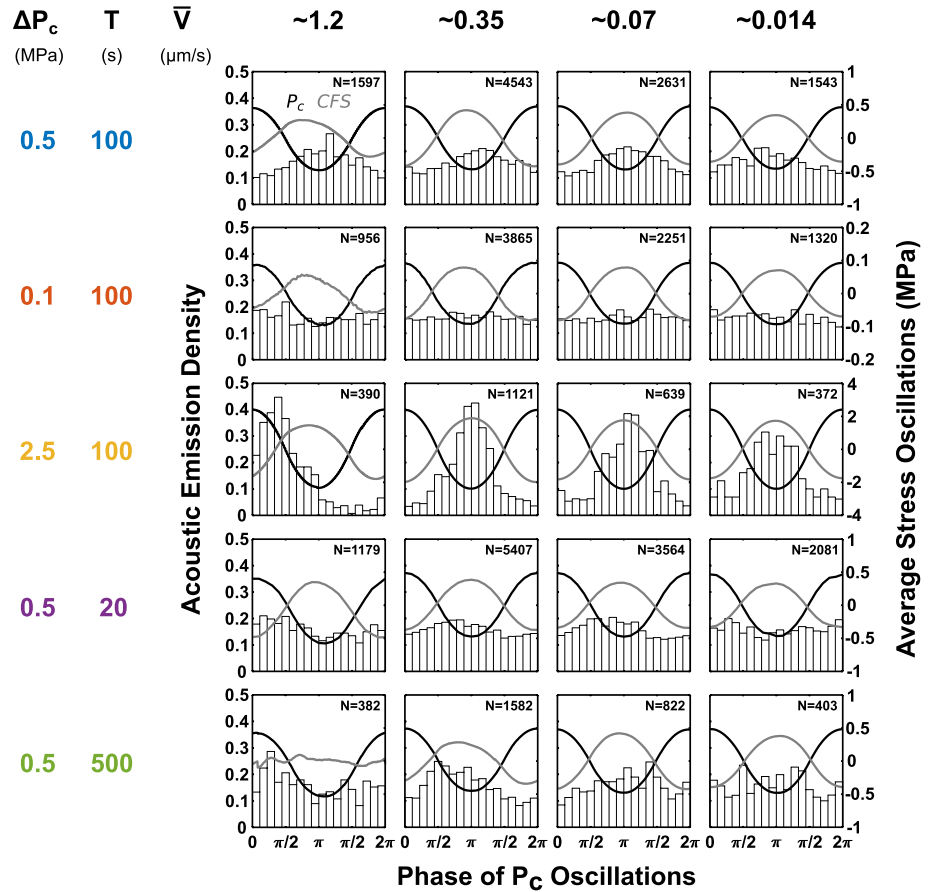


Figure 5. Acoustic emission phase distribution ($\phi = 0$ corresponds to the phase of maximum confining pressure), and detrended confining stress and Coulomb failure stress perturbations at corresponding phases averaged over the velocity segment. The different columns presented herein correspond to the fused catalogs of acoustic emissions of segments of similar piston velocities, except for the 1 $\mu\text{m/s}$ segment for which only the second segment is presented as the first segment corresponds to a transient state of the system wherein the gouge is not yet fully compacted.

distributed set of starting stress distributed throughout the sample. The constant background loading rate imposed on our sample is considered equivalent to a constant uniform stressing rate, and harmonic stress oscillations in turn induce harmonic oscillations in the stressing rate.

Within this framework, the theoretical AE distribution can be easily derived (see Figure 7), and is controlled by a single dimensionless parameter \tilde{c} :

$$\tilde{c} = \frac{\Delta CFS}{C\dot{F}S_0T} \quad (11)$$

where ΔCFS is the amplitude of the Coulomb stress oscillation, $C\dot{F}S_0$ is the background Coulomb failure stressing rate, and T is the oscillation period. Assuming a constant stiffness of the apparatus and sample, the background stress rate is proportional to the background loading rate V . Thus, for simplicity, we introduce the following parameter c :

$$c = \frac{\Delta CFS}{VT} \quad (12)$$

such that $c \propto \tilde{c}$. The parameter c is hereafter called the Coulomb stiffness because of its unit in MPa/m .

As we apply confining stress oscillations and axial loading, depending on the ratio of these loadings, our sample can experience both positive and negative Coulomb stressing rates. For positive Coulomb stressing rates, the probability density of the AE distribution is proportional to the instantaneous Coulomb stressing rate. If the Coulomb stressing rate is only positive, the average theoretical distribution of AEs is sinusoidal (Figures 7b–7e).

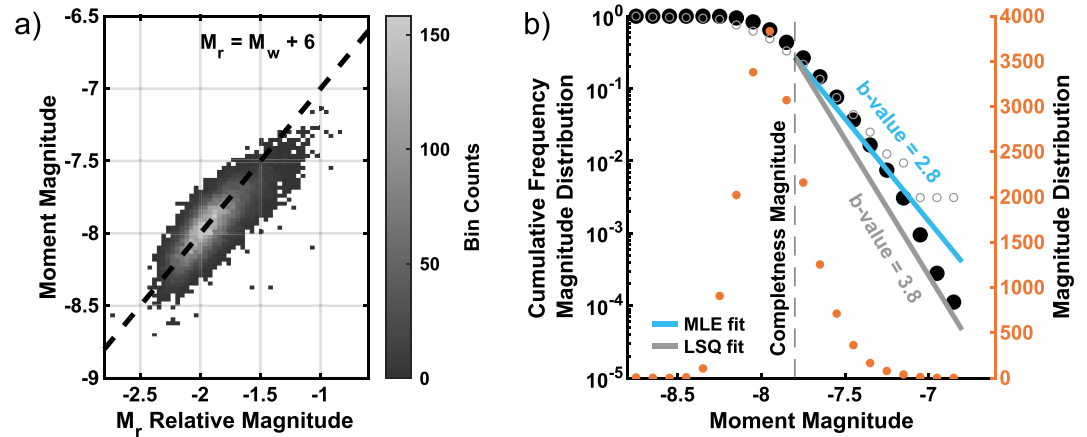


Figure 6. Magnitude distributions in Experiment n°1 ($\Delta P_c = 0.5$ MPa, $T = 100$ s). (a) Absolute moment magnitudes against Root Mean Square (RMS) relative magnitudes M_r . A line of slope 1 is provided for guidance to show that both magnitude evaluations are in agreement and are linearly bound. (b) Cumulative Frequency-Magnitude Distribution of the RMS relative magnitudes (expressed as absolute moment magnitudes considering the relation derived in panel a), for acoustic emissions (AEs) for which the absolute magnitude is also calculated (closed black circles, $N = 17,832$ AEs), and for AEs for which it is not possible to determine the absolute magnitude (open gray circles, $N = 320$ AEs). For other experiments, the number of emissions for which the absolute magnitude could not be calculated can reach represent a significant portion of the AEs. The non-cumulative Magnitude Distribution of all events is also presented to illustrate the conservativeness of the completeness magnitude estimate of -7.8 . GR law fits obtained through the least squares method (gray) and maximum likelihood estimations (blue) and using the events for which the absolute magnitude is calculated are also displayed. These are representative of all experiments.

For negative Coulomb stressing rates, also known as stress reversal, the phases of the oscillations during which the stress reversal occurs exhibit quiescence, that is, an absence of AEs, as the nucleation stress threshold is not reached (Figure 7f). In the case of stress reversal, the probability density of the AE distribution is equal to zero until the Coulomb stress reaches its previous maximum value.

The response amplitude s of the AE distribution directly correlates with the Coulomb stiffness, such that first order theoretical properties can be derived:

1. For a given value of the Coulomb stiffness, the response amplitude should be constant.
2. The response amplitude increases with the Coulomb stiffness.
3. Quiescence should be observed whenever stress reversal is present.

Due to the complex geometry of our experimental system and to the oscillations of both normal and shear stresses on the fault, the notion of stress reversal relates to oscillations of the Coulomb failure stress, defined as follows:

$$CFS = \tau - \mu' \sigma_N \quad (13)$$

where μ' is the static friction coefficient. Assuming $\mu' = 0.7$, a value close to that reached by the effective friction coefficient by the end of each of our experiments and comparable to that reported by the literature (e.g., Scholz et al., 2019), the Coulomb stress oscillates and displays stress reversal during almost every velocity segment (Figure S8 in Supporting Information S1). This is in line with tidal stress oscillations, which very commonly induce stress reversal (Beeler & Lockner, 2003; Heaton, 1982). An important assumption made here is that the shear and normal stresses at a macroscopic scale apply at a microscopic scale. Indeed, the stress field within the gouge is heterogeneous at the grain scale and highly dependent on the geometry of gouge grains and grain boundaries. However, we are unable to measure stress at this scale and must therefore rely on macroscopic stress, which gives us an average value of the stress throughout the sample.

The amplitude of the Coulomb stress oscillations is proportional to the amplitude of the imposed confining pressure oscillations, such that $\Delta CFS = 0.7 \Delta P_c$ as observed in Figure 5. Therefore, the Coulomb stiffness can be expressed as follows:

$$c \propto \frac{\Delta P_c}{VT} \quad (14)$$

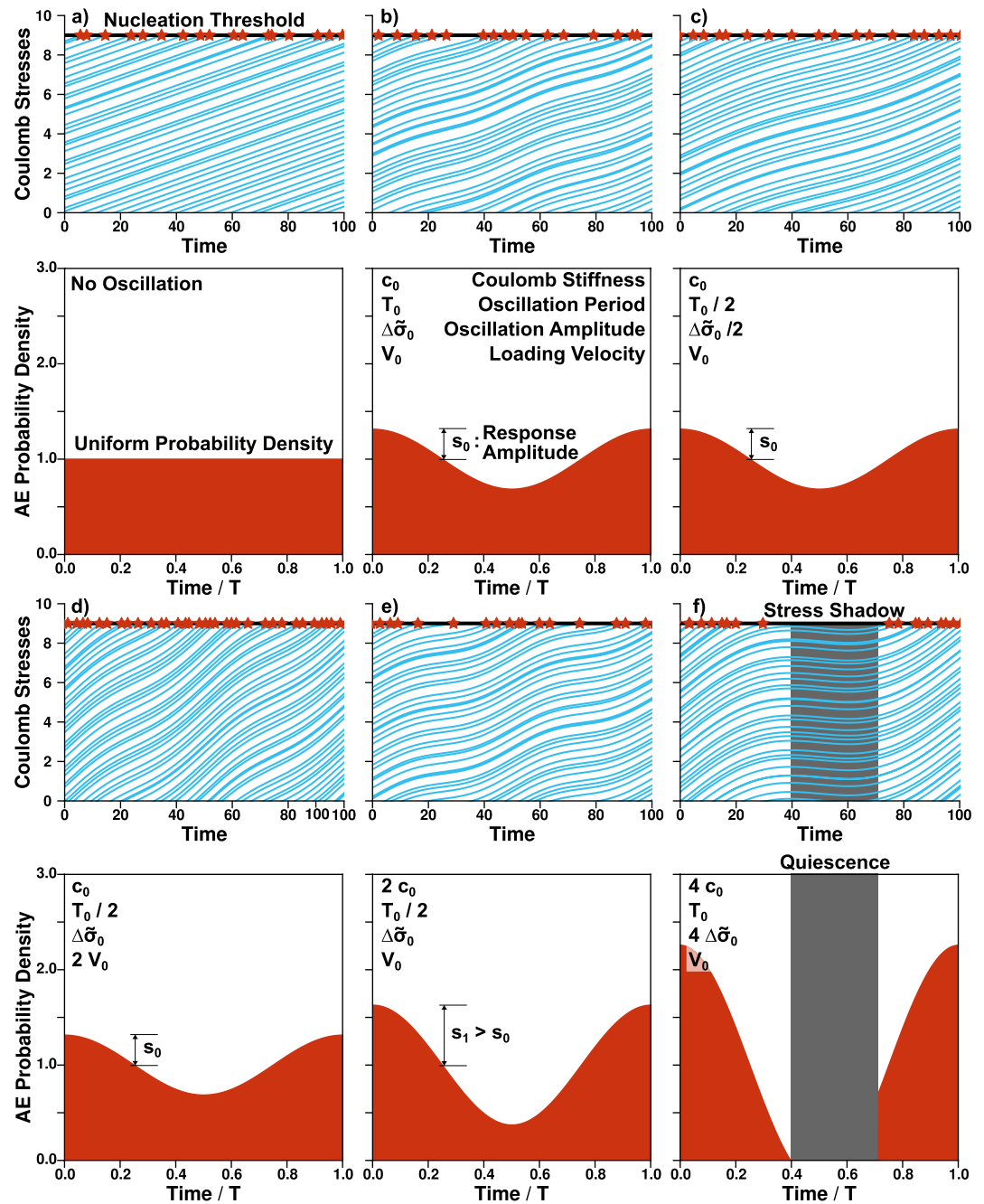


Figure 7. Coulomb failure model illustration for acoustic emission (AE) triggering and modulation of AE PDF (inspired by Beeler & Lockner, 2003; Heki, 2003). (a) Top: Considering a medium where Coulomb stress is locally dissipated through ruptures in a stochastic process, one can consider Coulomb stress in the medium, represented here by blue curves, to be randomly distributed. A positive stressing rate corresponding to a loading velocity V causes the Coulomb stress to increase throughout the medium. Once Coulomb stress reaches a stress threshold, it is released through an AE. Bottom: A constant loading rate results in a uniform AE probability density. (b) A sinusoidal Coulomb stress oscillation added to a background loading rate results in a sinusoidal response of the AE distribution. (c and d) Any oscillation and background loading rate that conserve the same Coulomb stiffness result in an identical AE distribution. (e) A larger Coulomb stiffness results in a larger response amplitude. (f) Negative stressing rates prevent nucleation. This leads to characteristic phases of quiescence.

Focusing on the amplitude of stress oscillations rather than on the amplitude of Coulomb stress oscillations allows the comparison with other experiments for which the Coulomb stress oscillation amplitudes are not known. More specifically, experiments in the literature use imposed pore fluid pressure P_f oscillations (Chanard et al., 2019;

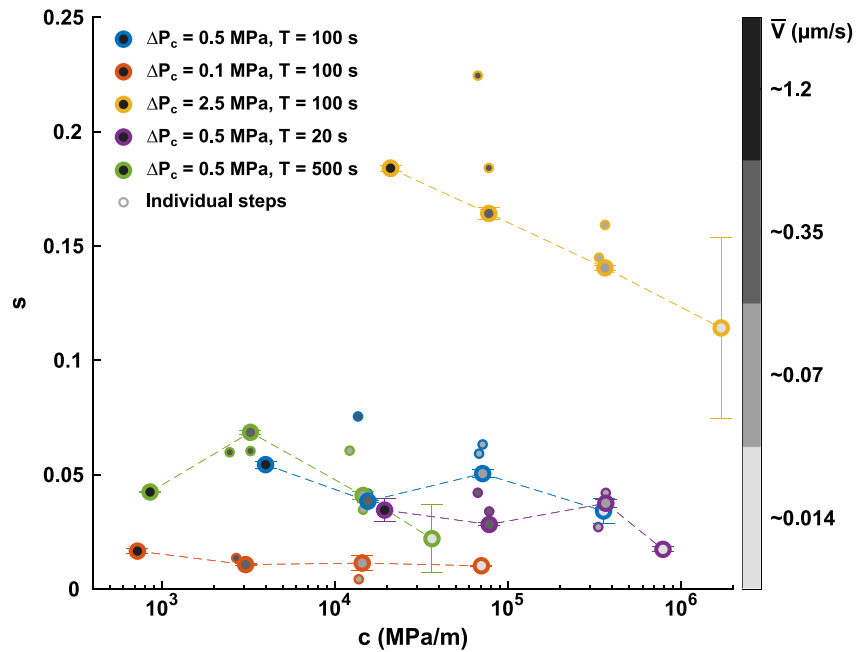


Figure 8. Response amplitude (s) of the acoustic emission (AE) distribution during velocity segment as a function of the Coulomb stiffness (c in MPa/m). Small symbols correspond to the response amplitude of AE catalogs during each velocity segment. Larger symbols linked by dashed lines correspond to the response amplitude of AE catalogs for which ascending and descending velocity segments are merged. Due to its transient nature, the very first segment of each experiment is always excluded, thus the 1 $\mu\text{m/s}$ data points correspond to the final experimental segments only. Error bars correspond to the standard deviation of the response amplitudes when calculated for AE catalogs divided into equal thirds, representative of each velocity.

Noël, Passelègue, et al., 2019; Noël, Pimienta, & Violay, 2019). Considering constant average values of shear and normal stress, the resulting Coulomb stress oscillations are derived (Beeler et al., 2000) as follows:

$$\Delta CFS = \mu' \Delta P_f \quad (15)$$

Thus, considering a static friction coefficient of 0.7, the Coulomb stiffness can be generalized as follows:

$$c \propto \frac{\Delta \tilde{\sigma}}{VT} \quad (16)$$

with $\Delta \tilde{\sigma}$ the imposed stress oscillation amplitude (either ΔP_c or ΔP_f).

Sinusoidal least squares fits of fixed periods of the AE phase histograms are calculated, the amplitudes of which are used as proxies for the response amplitude of the AE distribution. Interestingly, our experimental results (Figure 8) do not match the theoretical properties of the Coulomb Failure model. The response amplitude is not directly correlated to the Coulomb stiffness, the influence of the stress oscillation amplitude being much greater than the influence of the oscillation period for instance, with increases in oscillation amplitude resulting in large increases in response amplitude. Moreover, the influence of velocity is the opposite of the model prediction, as increasing velocity leads to increases in response amplitude. Finally, no consistent period of quiescence is observed in our experiments, despite most of our experimental velocity segments containing stress reversal.

Moreover, the velocity segments where stress reversal occurs the most correspond to the lowest velocity segments, which also happen to be the velocity segments where the response amplitude is at its lowest within each experiment. This implies that at lower velocities, the AE rate becomes oscillation-independent. This could be due to the complex geometry of the stress field within the gouge. Stress oscillations may induce local stress heterogeneities, which may promote nucleation during macroscopic stress reversals. At larger periods and slower velocities, greater viscoelastic relaxation of stress through creep may also take place. Such creep could in turn lead to increased background AE-rates (according to the “preslip” model of earthquake nucleation; Beroza & Ellsworth, 1996) that would also work against any shear stress build-up. This could also be due to the lower

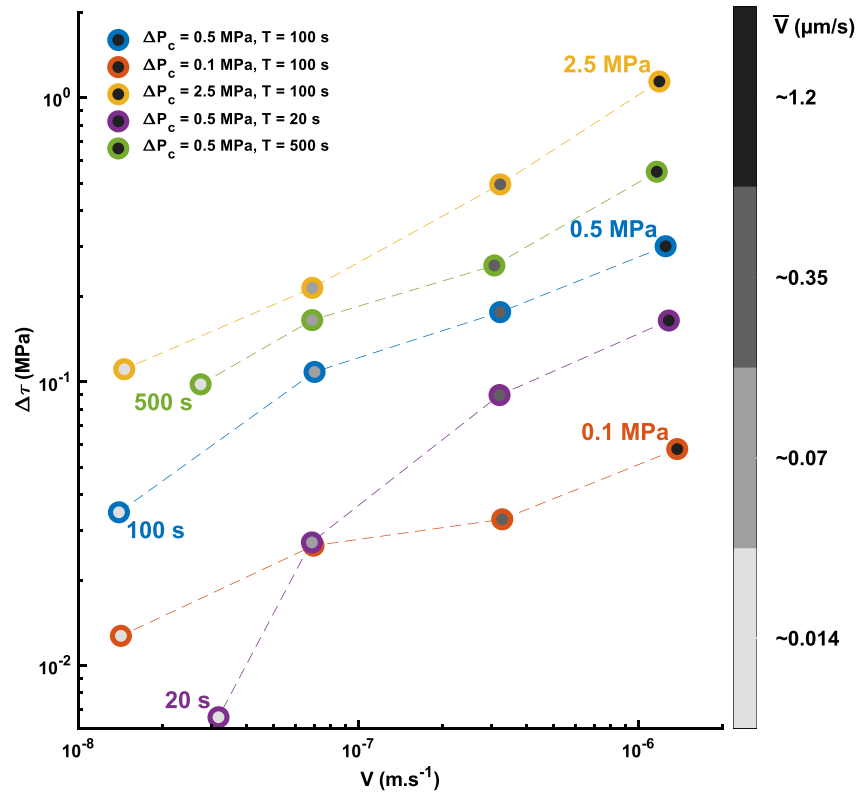


Figure 9. Evolution of the amplitude of the shear stress oscillations ($\Delta\tau$ in MPa) with slip velocity (V in m.s^{-1}). The amplitude of the shear stress oscillations is derived by fitting the mean shear stress over one oscillation by a sinusoid of fixed period. The amplitude of the shear stress oscillations increases with velocity, and with both pressure oscillation amplitude and period, indicating that the imposed stress oscillations do not overall translate to equivalent shear stress oscillations on the fault plane.

phase clustering of AEs at low velocities, which could allow less shear stress build-up throughout the oscillation (Figure 9). These observations could also signify that our experiments are mostly conducted in the high-frequency regime described earlier.

This hypothesis is also supported by the phase of AEs. In most experimental segments, the preferential occurrence phase of AE correlates positively with the phase of greatest Coulomb stress. This is not in line with the Mohr-Coulomb failure model, which predicts that AEs should nucleate preferentially at phases of greatest stressing rate. The only segments where the correlation with the greatest Coulomb stress occurs are the highest velocity segments in the experiments with either the largest oscillation amplitude or the largest oscillation period. This is in line with the theory of two nucleation-time-dependent regimes, as initially described by Dieterich (1987). Both experimental (Beeler & Lockner, 2003) and numerical (Dublanche, 2022) observations reproduce these behaviors. Likewise, our experiments are done around the transition between the two nucleation regimes.

4.2. Susceptibility of the AE Distribution Response Amplitude to Stress Oscillation Amplitude

For moderate stress oscillation amplitudes, numerical Burridge-Knopoff simulations (Pétreils et al., 2021) observe a linear relation between the response amplitude of the AE distribution and the oscillation amplitude such that:

$$s \propto \Delta\tilde{\sigma} \quad (17)$$

Calculating the susceptibility of the response amplitude to the confining pressure amplitude $\chi(\Delta\tilde{\sigma})$, that is, the response amplitude divided by the stress oscillation amplitude:

$$\chi(\Delta\tilde{\sigma}) = \frac{s}{\Delta\tilde{\sigma}} \quad (18)$$

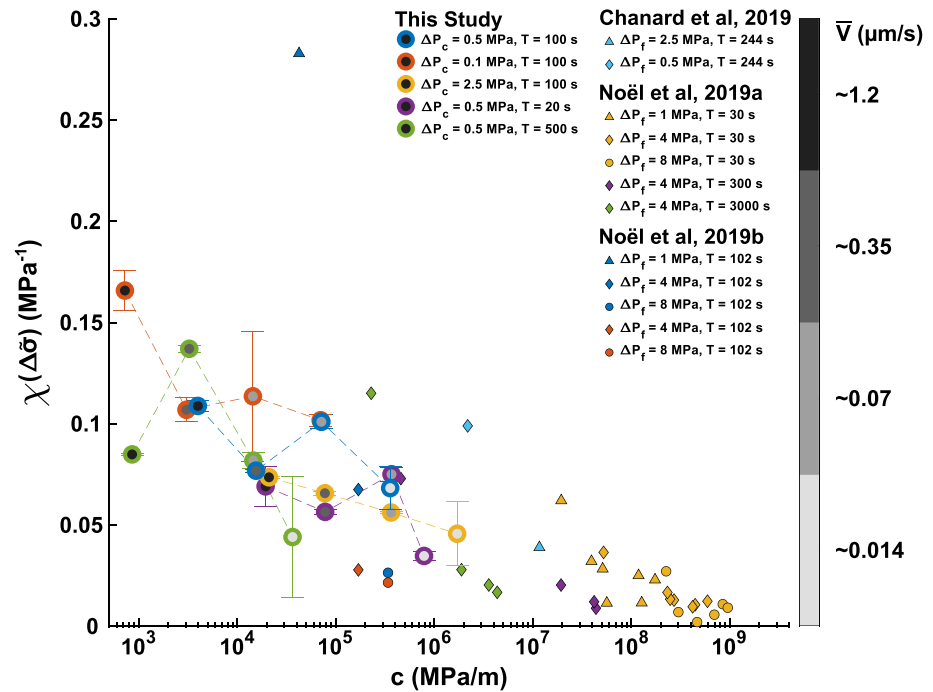


Figure 10. Susceptibility of the response amplitude of the acoustic emission distribution (χ) to the imposed stress oscillations amplitude ($\Delta\tilde{\sigma}$, either pore pressure or confining pressure oscillation amplitude) as defined in Equation 18, as a function of the Coulomb stiffness (c). Experimental results using data from Chanard et al. (2019), Noël, Passelègue, et al. (2019), and Noël, Pimienta, and Violay (2019) are also presented.

a first-order relationship relative to the Coulomb stiffness is made apparent (Figure 10), confirming as a first-order approximation the linear scaling of the response amplitude with the oscillation amplitude.

Furthermore, data from studies involving competition between fluid-induced pore pressure oscillations and axial loading with different experimental conditions and setups to this study's (Chanard et al., 2019; Noël, Passelègue, et al., 2019; Noël, Pimienta, & Violay, 2019) follow the same trend when the susceptibility of their response amplitudes to the pore pressure oscillation amplitude is plotted against Coulomb stiffness. This result is obtained despite other experiments being conducted with fluid pressure oscillations and using rock saw cuts as slip interfaces rather than gouge. The response amplitude for these experiments is derived following the same procedure as for this study's experiments.

4.3. Rate and State Friction Failure Model

The Coulomb Failure model fails to explain the distribution of AEs, let us now focus on the rate and state failure model. In this high-frequency regime, rate and state friction predict the seismicity rate to be independent of period and loading rate (Dieterich, 1994, 2007; Heimisson & Avouac, 2020). The rate and state model is most often times discussed in terms of seismicity rate R . Seismicity rate variations are similar to the response amplitude s used to quantify our experimental results, and as such, we consider that changes to the seismicity rate translate proportionally to changes in s .

In the rate and state friction failure model, the response in seismicity rate on how the oscillation period compares to the characteristic timescale t_a of response of the seismicity rate to stress perturbations with $t_a = A\sigma_N / C\dot{F}S_0$ where $C\dot{F}S_0$ is the background Coulomb loading rate. As our experiments change the loading rate of our system, t_a changes accordingly and varies between roughly 20 s during the fastest velocity segments and 5,000 s during the slowest velocity segments.

If $T < t_a$ then the seismicity rate response to small normal changes compared to the normal stress is:

$$R(t) = \frac{r}{M} \exp\left(\frac{CFS(t)}{A\sigma_N}\right) \quad (19)$$

with r the background seismicity rate when no stress oscillations are present and M is a scaling factor that does not change the amplitude of the AE distribution response. This approximation is however, only valid for $t \gg t_a$ (Heimisson & Avouac, 2020; Helmstetter & Shaw, 2009). As the mean AE rate is relatively constant in each of our velocity segments and as our velocity segments last for a duration far greater than t_a , we consider the conditions under which this expression of the seismicity rate is derived to be met when the oscillation period is shorter than t_a . In this case, following Heimisson and Avouac (2020), the AE response to the Coulomb stress oscillations can be expressed as follows:

$$R(t) = \frac{r}{M} \exp\left(\frac{\Delta CFS \sin(t)}{A\sigma_N}\right) \quad (20)$$

Considering our highest velocity segments where $t_a > T$, the susceptibility to oscillation amplitude of the AE distribution response is linear, as established in Section 4.2. This linearity is compatible with Equation 20 if $\Delta CFS \ll A\sigma_N$. This condition, however, does not seem to be met, as we estimate $A\sigma_N \sim 0.2$ MPa, with ΔCFS ranging from around 0.05 to 2 MPa. As such and considering that ΔCFS spans 2 orders of magnitude, we would expect an exponential response of the AE distribution to the oscillation amplitude, which we do not observe. This model also does not explain the dependence on loading velocity or oscillation period of susceptibility to the oscillation amplitude of the AE distribution.

The rate and state friction failure model does, however, describe that at $T > t_a$ the AE response correlates with the stressing rate and that at $T < t_a$ the AE response correlates with the stress. This is in line with Figure 5 where a correlation between the stressing rate and the AE distribution response is only observable at the highest loading rates and either highest period or oscillation loading rate where t_a is at its smallest.

The case of velocity strengthening stress and velocity oscillations was investigated by Ader et al. (2012) considering small Coulomb stress oscillation amplitude relative to $(a - b)\sigma_N$ and small velocity oscillation relative to the background loading rate. Neither the Coulomb stress oscillations nor the velocity oscillations present in our experiments correspond to the conditions considered by this study. Furthermore, as the velocity oscillation amplitude is larger than the background velocity, the slip velocity becomes negative during our stress oscillations. To the best of our knowledge, this is fundamentally incompatible with the rate and state framework and prohibits any solid investigation of the link between shear stress oscillations and velocity oscillation.

4.4. b -Value Modulation

Stress oscillations have been shown to have an influence on the magnitude-frequency distribution of natural seismicity (Ide et al., 2016; Scholz, 2015; Tan et al., 2019). An analysis of the variations of b -value throughout oscillations was thus undertaken using our experimental catalogs. All AEs except those contained in the first 1 mm of displacement of each experiment were here considered in order to have large enough catalogs for maximum likelihood b -value estimates to be statistically relevant.

AE sub-catalogs were defined for each experiment by selecting events within a given phase window. This phase window was then moved across the phase space to investigate the variations in b -value. The choice of the size of the phase windows induces a bias in the estimation of the b -values and the associated uncertainties. Larger phase windows contain a larger number of AEs and therefore are associated with smaller uncertainties, but variations of the b -value are smoothed out, whereas smaller phase windows contain fewer AEs and are therefore associated to larger uncertainties but do not suffer from as much smoothing of the variations of the b -value. A compromise thus had to be made when selecting a phase window size to highlight variations of b -values that are significant when compared with the associated uncertainties. The width of the phase window was here set to both π and $\pi/2$ to better evaluate the significance of the variations in b -value (Figure 11).

Oscillations in b -value are observable regardless of the imposed phase window width for experiments 1 ($\Delta P_c = 0.5$ MPa, $T = 100$ s) and 3 ($\Delta P_c = 2.5$ MPa, $T = 100$ s; see Figure S10 in Supporting Information S1). The amplitude of oscillation of the b -value increases with the stress oscillation amplitude, as observed in natural settings (e.g., Scholz, 2015; Tan et al., 2019). However, the different b -value oscillations are not in phase. According to numerical studies conducted on Burridge-Knopoff and Olami-Feder-Christensen models, b -value oscillations are expected when the modulation frequency is small enough. These b -value oscillation are in phase opposition with the normal stress oscillations (Pétreilis et al., 2021). However, our experimental results do not

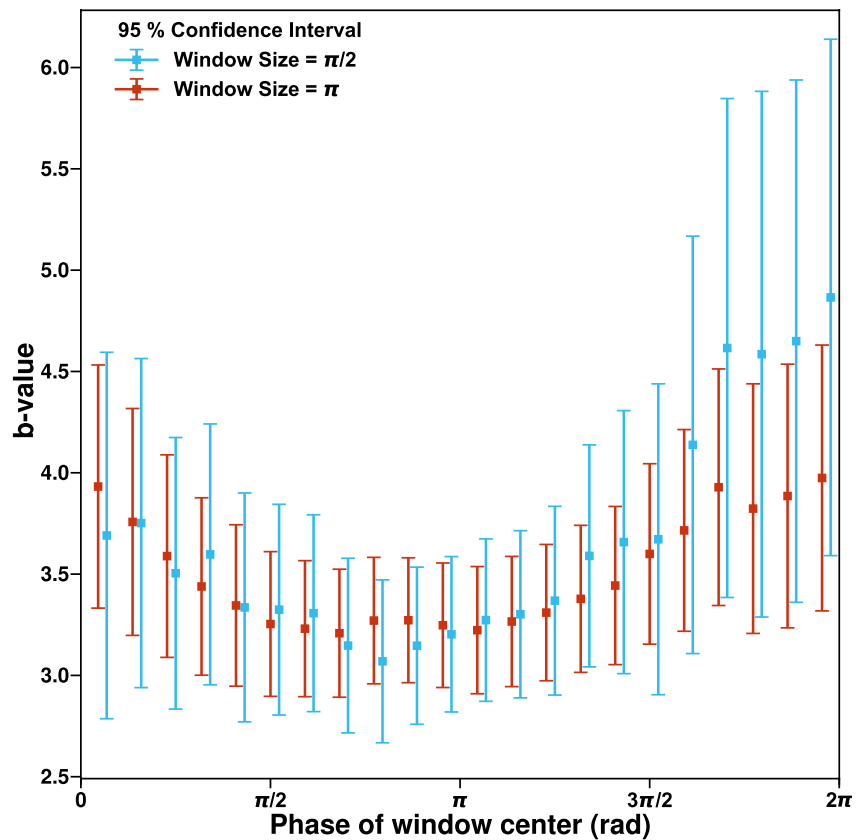


Figure 11. Gutenberg-Richter b -value calculated for acoustic emissions (AEs) within a moving phase window of π (red) or $\pi/2$ (blue) throughout Experiment n°3 ($\Delta P_c = 2.5$ MPa, $T = 100$ s). The b -value is determined with a maximum likelihood estimate.

conform to these numerical results and would require further investigation. The effect of the oscillation period on the b -value modulation is less clear. Indeed, for experiments conducted at $\Delta P_c = 0.5$ MPa, the error bars attached to the b -value oscillations are comparable in amplitude to the observable oscillations. Therefore, it is not possible to determine the dependence of the b -value oscillation amplitude to the oscillation period.

4.5. Relevance to Natural Oscillatory Stress Phenomena

Our experimental observations show an increase in microseismicity modulation primarily with increased stress oscillation amplitude as well as with both oscillation period and background loading rate. The increase in microseismicity modulation with stressing amplitude is in line with the natural case, where seismicity has robustly been shown to be triggered by large stress variations caused by seismic wave propagation (Brodsky & van der Elst, 2014), and more modestly modulated at longer periods by smaller amplitude of stress variations (e.g., Bollinger et al., 2007; Métivier et al., 2009). Moreover, the increase in modulation with loading period could explain why despite tidal and seasonal or multiannual stressing being of comparable amplitudes, tidal modulation is less commonly observed than seasonal and multiannual modulation (Beeler & Lockner, 2003). Interestingly, our experimental results also show the role of background loading rates in modulating seismicity, which seems consistent with larger-scale observations. Indeed, natural faults appear to express different levels of sensitivity to oscillating stresses, for example, at seasonal periods, with the best constrained modulations being witnessed in tectonic contexts with large strain rates such as the Himalayas (Bollinger et al., 2007) or Alaska (C. W. Johnson et al., 2020). In fact, similarly to experimental results, natural observations of triggered or modulated seismicity by various transient and oscillatory phenomena can be represented by the Coulomb stiffness as a function of the oscillation period, over more than 10 orders of magnitude (Figure 12). Within this framework, natural observations and experimental results of this study roughly fall in a range of constant $\Delta\tilde{\sigma}/V$. As such, the susceptibility of earthquake nucleation to stress oscillations in natural setting seems better probed by experiments applying

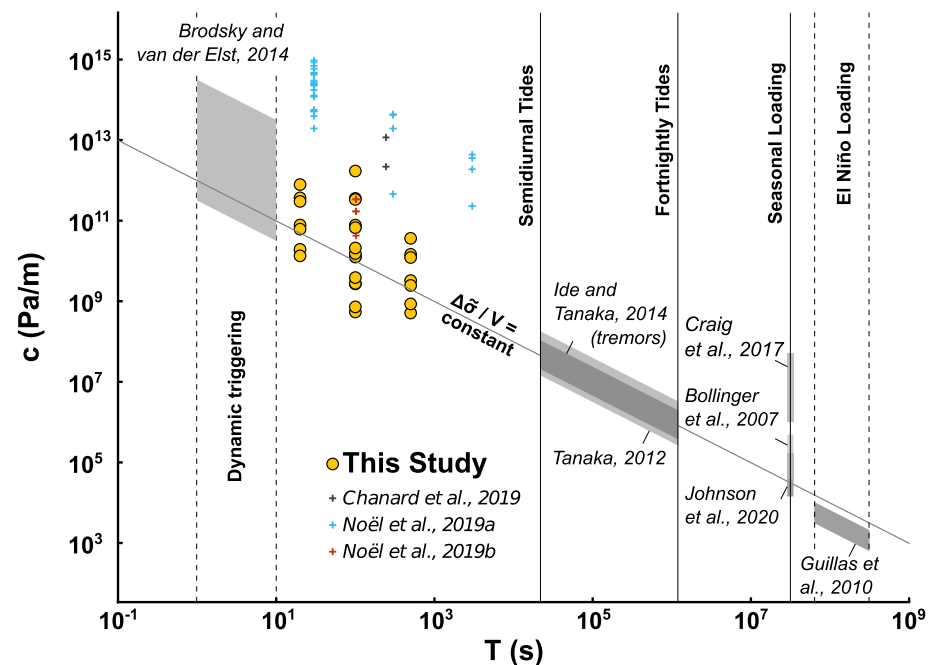


Figure 12. Coulomb stiffness as a function of oscillation period for experimental data and select natural seismicity observations from earthquake catalogs. In natural contexts with similar background stressing rates, stress oscillation of similar amplitudes, but different periods elicit different responses from seismogenic zones, for example, directly or delayed triggered seismicity, modulation of seismicity rate, or no observed correlation. Velocities are taken from the references shown in the figure. Periods and stress variations are given in Table S1 in Supporting Information S1.

small amplitude of stress oscillations. However, comparing experiments conducted by different studies is difficult due to different sample geometries, experimental procedures, and sample material. For instance, experiments conducted with intact rocks were conducted at higher $\Delta\tilde{\sigma}/V$ ratios than experiments using either faulted or gouge samples and higher $\tilde{\sigma}/V$ ratios than are usually observed in the natural setting but still present important results that could be applicable to systems that undergo small tectonic loading or particularly large stress oscillations.

The scaling of these observations is to be considered with caution. Indeed, the largest tectonic loading rates correspond to highly seismogenic zones (Ide, 2013) which deliver larger seismic catalogs and thereby make them more studied. Additionally, the seasonal modulation of seismicity in the New Madrid Seismic Zone (Craig et al., 2017) remains a troubling observation, as regional Global Navigation Satellite System (GNSS) observations do not indicate any large-scale deformation (Craig & Calais, 2014), although the seismicity could be explained by the presence of localized stress on and around specific faults not captured by the sparse GNSS network.

Experiments also indicate that an increase in the amplitude of GR b -value oscillation is correlated with an increase in stress oscillation amplitude, but experimental limitations preclude the quantification of a phase link between stress and b -value. Yet, this link is coherent with the few natural observations of b -value modulation by stress oscillations (Scholz, 2015; Tan et al., 2019). Given that larger magnitude events have larger nucleation times (Ohnaka, 2000), it would be expected that the response regime of earthquakes to stress oscillations would be magnitude-dependent. This could explain the b -value variations with stress oscillations and is in line with observations in the natural case where differential stress variations are linked to the b -value.

Some limitations of our experiments include assuming a fault geometry which is akin to that of thrust faults, these being the faults on which the modulation of earthquakes by periodic loading seems to be the most readily observed (Cochran et al., 2004; Ide et al., 2016; C. W. Johnson et al., 2017). It would be of interest to also consider the case of strike-slip geometries in the laboratory with an appropriate experimental device, to explore their response to different stressing conditions. Another experimental limitation of this work is the use of oscillation periods corresponding to the range between dynamic triggering and tidal characteristic Coulomb stiffness. The large oscillation periods of most natural oscillatory stress phenomena make experimental work with those periods difficult.

5. Conclusions

Confining pressure oscillations experiments—of amplitudes ranging from 0.1 to 2.5 MPa and periods ranging from 20 to 500 s—are conducted on gouge layers with a stress geometry associated with reverse faulting and undergoing slow axial stressing—inducing slip ranging from 1 $\mu\text{m/s}$ to 10 nm/s—to determine the modulation of microseismicity by stress oscillations in tectonic contexts. The resulting response amplitude of the microseismicity distribution is linearly susceptible to oscillation amplitude and increases with velocity. Our results mostly do not conform to the low-frequency Coulomb-failure regime, indicating that the considered oscillation periods are smaller than the nucleation times of microseismicity (here recorded in the form of AEs). The high-frequency rate and state regime also fails in explaining the linear susceptibility of the AE distribution response to stress oscillation amplitude despite the range of parameters probed. However, the susceptibility to stress amplitude does scale with the Coulomb stiffness. Moreover, we show that experimental results tend to follow the same Coulomb stiffness–period scaling law as natural seismicity linked to oscillatory phenomena. We experimentally confirm the absence of quiescence during stress reversal, probably linked to complex stress heterogeneities and viscoelastic relaxations taking place in our granular fault gouge medium. We also confirm the possibility of small oscillatory perturbations modulating the b -value, which is relevant to observations of tide-based modulation of seismicity b -value (Ide et al., 2016). Further investigation of the influence of stress oscillations on b -value could be useful for earthquake hazard assessment, as well as more experimental work to assess the response of AEs in both the high-frequency nucleation-driven regime and low-frequency threshold-driven regime. Finally, one important perspective of this work is to address the specific case of the response and susceptibility of a system undergoing stick-slip motion, for which the microseismicity might be clustered into foreshock-mainshock-after-shock sequences, in order to investigate further how the susceptibility evolves during the seismic cycle at the laboratory scale.

Data Availability Statement

The acoustic emission waveforms, mechanical data and derived data used to construct the figures in the study are available at [Zenodo.org](https://zenodo.org) via <https://doi.org/10.5281/zenodo.7786438> with a Creative Commons Attribution 4.0 International Licence.

Acknowledgments

The authors would like to thank Takahiro HATANO, Julien GASC, and Samson MARTY for valuable discussions and, in the case of the two latter, for providing some pre-existing Matlab codes that were used in this study. The authors would also like to thank the two anonymous reviewers and editors for their useful comments and suggestions. This work was supported by the LRC Yves Rocard (Laboratoire de Recherche Conventionné CEA-ENS-CNRS), the European Research Council Grant 681346 REALISM and the Centre National de la Recherche Scientifique via the program “Tellus-Aleas” of the Institut National des Sciences de l’Univers.

References

- Ader, T. J., Ampuero, J.-P., & Avouac, J.-P. (2012). The role of velocity-neutral creep on the modulation of tectonic tremor activity by periodic loading. *Geophysical Research Letters*, 39(16). <https://doi.org/10.1029/2012GL052326>
- Ader, T. J., & Avouac, J.-P. (2013). Detecting periodicities and declustering in earthquake catalogs using the Schuster spectrum, application to Himalayan seismicity. *Earth and Planetary Science Letters*, 377–378, 97–105. <https://doi.org/10.1016/j.epsl.2013.06.032>
- Adhikari, L. B., Bollinger, L., Vergne, J., Lambotte, S., Chanard, K., Laporte, M., et al. (2021). Orogenic collapse and stress adjustments revealed by an intense seismic swarm following the 2015 Gorkha earthquake in Nepal. *Frontiers of Earth Science*, 524. <https://doi.org/10.3389/feart.2021.659937>
- Aki, K. (1965). Maximum likelihood estimate of b in the formula $\log N = a - bM$ and its confidence limits. *Bulletin of Earthquake Research Institute*, 43, 237–239.
- Ampuero, J.-P., & Rubin, A. M. (2008). Earthquake nucleation on rate and state faults—Aging and slip laws. *Journal of Geophysical Research: Solid Earth*, 113(B1), B01302. <https://doi.org/10.1029/2007JB005082>
- Anderson, J. G., Brune, J. N., Louie, J. N., Zeng, Y., Savage, M., Yu, G., et al. (1994). Seismicity in the western Great Basin apparently triggered by the Landers, California, earthquake, 28 June 1992. *Bulletin of the Seismological Society of America*, 84(3), 863–891. <https://doi.org/10.1785/BSSA0840030863>
- Bachmann, C. E., Wiemer, S., Goertz-Allmann, B. P., & Woessner, J. (2012). Influence of pore-pressure on the event-size distribution of induced earthquakes. *Geophysical Research Letters*, 39(9). <https://doi.org/10.1029/2012GL051480>
- Bartlow, N. M., Lockner, D. A., & Beeler, N. M. (2012). Laboratory triggering of stick-slip events by oscillatory loading in the presence of pore fluid with implications for physics of tectonic tremor. *Journal of Geophysical Research: Solid Earth*, 117(B11). <https://doi.org/10.1029/2012JB009452>
- Bedford, J. D., Faulkner, D. R., & Lapusta, N. (2022). Fault rock heterogeneity can produce fault weakness and reduce fault stability. *Nature Communications*, 13(1), 326. <https://doi.org/10.1038/s41467-022-27998-2>
- Beeler, N. M., & Lockner, D. A. (2003). Why earthquakes correlate weakly with the solid Earth tides: Effects of periodic stress on the rate and probability of earthquake occurrence. *Journal of Geophysical Research: Solid Earth*, 108(B8), 2391. <https://doi.org/10.1029/2001JB001518>
- Beeler, N. M., Simpson, R. W., Hickman, S. H., & Lockner, D. A. (2000). Pore fluid pressure, apparent friction, and Coulomb failure. *Journal of Geophysical Research: Solid Earth*, 105(B11), 25533–25542. <https://doi.org/10.1029/2000JB900119>
- Beeler, N. M., Tullis, T. E., Blanpied, M. L., & Weeks, J. D. (1996). Frictional behavior of large displacement experimental faults. *Journal of Geophysical Research: Solid Earth*, 101(B4), 8697–8715. <https://doi.org/10.1029/96JB00411>
- Beroza, G. C., & Ellsworth, W. L. (1996). Properties of the seismic nucleation phase. *Tectonophysics*, 261(1), 209–227. [https://doi.org/10.1016/0040-1951\(96\)00067-4](https://doi.org/10.1016/0040-1951(96)00067-4)

- Bettinelli, P., Avouac, J.-P., Flouzat, M., Bollinger, L., Ramillien, G., Rajauri, S., & Sapkota, S. (2008). Seasonal variations of seismicity and geodetic strain in the Himalaya induced by surface hydrology. *Earth and Planetary Science Letters*, 266(3–4), 332–344. <https://doi.org/10.1016/j.epsl.2007.11.021>
- Bollinger, L., Perrier, F., Avouac, J.-P., Sapkota, S., Gautam, U., & Tiwari, D. R. (2007). Seasonal modulation of seismicity in the Himalaya of Nepal. *Geophysical Research Letters*, 34(8). <https://doi.org/10.1029/2006GL029192>
- Bolton, D. C., Shokouhi, P., Rouet-Leduc, B., Hulbert, C., Rivière, J., Marone, C., & Johnson, P. A. (2019). Characterizing acoustic signals and searching for precursors during the laboratory seismic cycle using unsupervised machine learning. *Seismological Research Letters*, 90(3), 1088–1098. <https://doi.org/10.1785/0220180367>
- Bolton, D. C., Shreedharan, S., McLaskey, G. C., Rivière, J., Shokouhi, P., Trugman, D. T., & Marone, C. (2022). The high-frequency signature of slow and fast laboratory earthquakes. *Journal of Geophysical Research: Solid Earth*, 127(6), e2022JB024170. <https://doi.org/10.1029/2022JB024170>
- Bourbie, T., & Zinszner, B. (1985). Hydraulic and acoustic properties as a function of porosity in Fontainebleau Sandstone. *Journal of Geophysical Research*, 90(B13), 11524. <https://doi.org/10.1029/JB090iB13p11524>
- Brantut, N., Schubnel, A., & Guéguen, Y. (2011). Damage and rupture dynamics at the brittle-ductile transition: The case of gypsum. *Journal of Geophysical Research: Solid Earth*, 116(B1), B01404. <https://doi.org/10.1029/2010jb007675>
- Brodsky, E. E., & van der Elst, N. J. (2014). The uses of dynamic earthquake triggering. *Annual Review of Earth and Planetary Sciences*, 42(1), 317–339. <https://doi.org/10.1146/annurev-earth-060313-054648>
- Chanard, K., Nicolas, A., Hatano, T., Petrelis, F., Latour, S., Vinciguerra, S., & Schubnel, A. (2019). Sensitivity of acoustic emission triggering to small pore pressure cycling perturbations during brittle creep. *Geophysical Research Letters*, 46(13), 7414–7423. <https://doi.org/10.1029/2019GL082093>
- Chelidze, T., Matcharashvili, T., Lursmanashvili, O., Varamashvili, N., Zhukova, N., & Meparidze, E. (2010). Triggering and synchronization of stick-slip: Experiments on spring-slider system. In *Synchronization and triggering: From fracture to earthquake processes* (pp. 123–164). Springer.
- Chen, K. H., Tai, H.-J., Ide, S., Byrne, T. B., & Johnson, C. W. (2018). Tidal modulation and tectonic implications of tremors in Taiwan. *Journal of Geophysical Research: Solid Earth*, 123(7), 5945–5964. <https://doi.org/10.1029/2018jb015663>
- Cochran, E. S., Vidale, J. E., & Tanaka, S. (2004). Earth tides can trigger shallow thrust fault earthquakes. *Science*, 306(5699), 1164–1166. <https://doi.org/10.1126/science.1103961>
- Craig, T. J., & Calais, E. (2014). Strain accumulation in the New Madrid and Wabash Valley seismic zones from 14 yr of continuous GPS observation. *Journal of Geophysical Research: Solid Earth*, 119(12), 9110–9129. <https://doi.org/10.1002/2014JB011498>
- Craig, T. J., Chanard, K., & Calais, E. (2017). Hydrologically-driven crustal stresses and seismicity in the New Madrid Seismic Zone. *Nature Communications*, 8(1), 2143. <https://doi.org/10.1038/s41467-017-01696-w>
- Davison, C. (1938). *Studies on the periodicity of earthquakes*. T. Murby & Company.
- Dieterich, J. H. (1981). Constitutive properties of faults with simulated gouge. In *Mechanical behavior of crustal rocks* (pp. 103–120). American Geophysical Union (AGU). <https://doi.org/10.1029/GM024p0103>
- Dieterich, J. H. (1987). Nucleation and triggering of earthquake slip: Effect of periodic stresses. *Tectonophysics*, 144(1), 127–139. [https://doi.org/10.1016/0040-1951\(87\)90012-6](https://doi.org/10.1016/0040-1951(87)90012-6)
- Dieterich, J. H. (1994). A constitutive law for rate of earthquake production and its application to earthquake clustering. *Journal of Geophysical Research: Solid Earth*, 99(B2), 2601–2618. <https://doi.org/10.1029/93JB02581>
- Dieterich, J. H. (2007). Applications of rate- and state-dependent friction to models of fault-slip and earthquake occurrence. In G. Schubert (Ed.), *Treatise on geophysics* (2nd ed., pp. 93–110). Elsevier. <https://doi.org/10.1016/B978-0-444-53802-4.00075-0>
- Dublanche, P. (2022). Seismicity modulation in a 3-D rate-and-state interacting fault population model. *Geophysical Journal International*, 229(3), 1804–1823. <https://doi.org/10.1093/gji/ggac023>
- Fortin, J., Guéguen, Y., & Schubnel, A. (2007). Effects of pore collapse and grain crushing on ultrasonic velocities and Vp/Vs. *Journal of Geophysical Research: Solid Earth*, 112(B8), B08207. <https://doi.org/10.1029/2005JB004005>
- Gasior, M., & Gonzalez, J. L. (2004). Improving FFT frequency measurement resolution by parabolic and Gaussian spectrum interpolation. *AIP Conference Proceedings*, 732(1), 276–285. <https://doi.org/10.1063/1.1831158>
- Geffers, G.-M., Main, I. G., & Naylor, M. (2022). Biases in estimating *b*-values from small earthquake catalogs: How high are high *b*-values? *Geophysical Journal International*, 229(3), 1840–1855. <https://doi.org/10.1093/gji/ggac028>
- Hartzell, S., & Heaton, T. (1989). The fortnightly tide and the tidal triggering of earthquakes. *Bulletin of the Seismological Society of America*, 79(4), 1282–1286. <https://doi.org/10.1785/bssa0790041282>
- Hawthorne, J. C., & Rubin, A. M. (2010). Tidal modulation of slow slip in Cascadia. *Journal of Geophysical Research: Solid Earth*, 115(B9), B09406. <https://doi.org/10.1029/2010JB007502>
- Heaton, T. H. (1982). Tidal triggering of earthquakes. *Bulletin of the Seismological Society of America*, 72(6A), 2181–2200. <https://doi.org/10.1785/BSSA07206A2181>
- Heimisson, E. R., & Avouac, J.-P. (2020). Analytical prediction of seismicity rate due to tides and other oscillating stresses. *Geophysical Research Letters*, 47(23), e2020GL090827. <https://doi.org/10.1029/2020GL090827>
- Heki, K. (2003). Snow load and seasonal variation of earthquake occurrence in Japan. *Earth and Planetary Science Letters*, 207(1–4), 159–164. [https://doi.org/10.1016/S0012-821X\(02\)01148-2](https://doi.org/10.1016/S0012-821X(02)01148-2)
- Helmstetter, A., & Shaw, B. E. (2009). Afterslip and aftershocks in the rate-and-state friction law. *Journal of Geophysical Research: Solid Earth*, 114(B1). <https://doi.org/10.1029/2007JB005077>
- Hill, D. P., Reasenber, P. A., Michael, A., Arabaz, W. J., Beroza, G., Brumbaugh, D., et al. (1993). Seismicity remotely triggered by the magnitude 7.3 Landers, California, earthquake. *Science*, 260(5114), 1617–1623. <https://doi.org/10.1126/science.260.5114.1617>
- Hsu, Y.-J., Kao, H., Bürgmann, R., Lee, Y.-T., Huang, H.-H., Hsu, Y.-F., et al. (2021). Synchronized and asynchronous modulation of seismicity by hydrological loading: A case study in Taiwan. *Science Advances*, 7(16), eabf7282. <https://doi.org/10.1126/sciadv.abf7282>
- Ide, S. (2013). The proportionality between relative plate velocity and seismicity in subduction zones. *Nature Geoscience*, 6(9), 780–784. <https://doi.org/10.1038/ngeo1901>
- Ide, S., & Tanaka, Y. (2014). Controls on plate motion by oscillating tidal stress: Evidence from deep tremors in western Japan: Ide et al. Plate Motion by Tidal Stress. *Geophysical Research Letters*, 41(11), 3842–3850. <https://doi.org/10.1002/2014GL060035>
- Ide, S., Yabe, S., & Tanaka, Y. (2016). Earthquake potential revealed by tidal influence on earthquake size-frequency statistics. *Nature Geoscience*, 9(11), 834–837. <https://doi.org/10.1038/ngeo2796>
- Johnson, C. W., Fu, Y., & Bürgmann, R. (2017). Seasonal water storage, stress modulation, and California seismicity. *Science*, 356(6343), 1161–1164. <https://doi.org/10.1126/science.aak9547>

- Johnson, C. W., Fu, Y., & Bürgmann, R. (2020). Hydrospheric modulation of stress and seismicity on shallow faults in southern Alaska. *Earth and Planetary Science Letters*, 530, 115904. <https://doi.org/10.1016/j.epsl.2019.115904>
- Johnson, P. A., Ferdowsi, B., Kaproth, B. M., Scuderi, M., Griffa, M., Carmeliet, J., et al. (2013). Acoustic emission and microslip precursors to stick-slip failure in sheared granular material. *Geophysical Research Letters*, 40(21), 5627–5631. <https://doi.org/10.1002/2013gl057848>
- Johnson, P. A., & Jia, X. (2005). Nonlinear dynamics, granular media, and dynamic earthquake triggering. *Nature*, 437(7060), 871–874. <https://doi.org/10.1038/nature04015>
- Johnson, P. A., Savage, H., Knuth, M., Gombert, J., & Marone, C. (2008). Effects of acoustic waves on stick-slip in granular media and implications for earthquakes. *Nature*, 451(7174), 57–60. <https://doi.org/10.1038/nature06440>
- Klein, F. W. (1976). Earthquake swarms and the semidiurnal solid Earth tide. *Geophysical Journal International*, 45(2), 245–295. <https://doi.org/10.1111/j.1365-246X.1976.tb00326.x>
- Knopoff, L. (1964). Earth tides as a triggering mechanism for earthquakes. *Bulletin of the Seismological Society of America*, 54(6A), 1865–1870. <https://doi.org/10.1785/BSSA05406A1865>
- Leeman, J. R., Saffer, D. M., Scuderi, M. M., & Marone, C. (2016). Laboratory observations of slow earthquakes and the spectrum of tectonic fault slip modes. *Nature Communications*, 7(1), 11104. <https://doi.org/10.1038/ncomms11104>
- Linker, M. F., & Dieterich, J. H. (1992). Effects of variable normal stress on rock friction: Observations and constitutive equations. *Journal of Geophysical Research*, 97(B4), 4923. <https://doi.org/10.1029/92JB00017>
- Lockner, D. A. (1993). The role of acoustic emission in the study of rock fracture. *International Journal of Rock Mechanics and Mining Sciences & Geomechanics Abstracts*, 30(7), 883–899. [https://doi.org/10.1016/0148-9062\(93\)90041-B](https://doi.org/10.1016/0148-9062(93)90041-B)
- Lockner, D. A., & Beeler, N. M. (1999). Premonitory slip and tidal triggering of earthquakes. *Journal of Geophysical Research: Solid Earth*, 104(B9), 20133–20151. <https://doi.org/10.1029/1999JB900205>
- Madariaga, R. (1976). Dynamics of an expanding circular fault. *Bulletin of the Seismological Society of America*, 66(3), 639–666. <https://doi.org/10.1785/bssa0660030639>
- Mair, K., Marone, C., & Young, R. P. (2007). Rate dependence of acoustic emissions generated during shear of simulated fault gouge. *Bulletin of the Seismological Society of America*, 97(6), 1841–1849. <https://doi.org/10.1785/0120060242>
- Marone, C. (1998). Laboratory-derived friction laws and their application to seismic faulting. *Annual Review of Earth and Planetary Sciences*, 26(1), 643–696. <https://doi.org/10.1146/annurev.earth.26.1.643>
- Marone, C., Raleigh, C. B., & Scholz, C. H. (1990). Frictional behavior and constitutive modeling of simulated fault gouge. *Journal of Geophysical Research: Solid Earth*, 95(B5), 7007–7025. <https://doi.org/10.1029/JB095iB05p07007>
- Marone, C., & Scholz, C. H. (1989). Particle-size distribution and microstructures within simulated fault gouge. *Journal of Structural Geology*, 11(7), 799–814. [https://doi.org/10.1016/0191-8141\(89\)90099-0](https://doi.org/10.1016/0191-8141(89)90099-0)
- Marty, S. (2020). High-frequency radiation and foreshocks during laboratory earthquakes, (Unpublished doctoral dissertation). ENS.
- Marzocchi, W., Spassiani, I., Stallone, A., & Taroni, M. (2020). How to be fooled searching for significant variations of the *b*-value. *Geophysical Journal International*, 220(3), 1845–1856. <https://doi.org/10.1093/gji/ggz541>
- Meredith, P. G., Main, I. G., & Jones, C. (1990). Temporal variations in seismicity during quasi-static and dynamic rock failure. *Tectonophysics*, 175(1), 249–268. [https://doi.org/10.1016/0040-1951\(90\)90141-T](https://doi.org/10.1016/0040-1951(90)90141-T)
- Métivier, L., de Viron, O., Conrad, C. P., Renault, S., Diamant, M., & Patau, G. (2009). Evidence of earthquake triggering by the solid Earth tides. *Earth and Planetary Science Letters*, 278(3–4), 370–375. <https://doi.org/10.1016/j.epsl.2008.12.024>
- Mogi, K. (1962). *Study of elastic shocks caused by the fracture of heterogeneous materials and its relations to earthquake phenomena* (pp. 125–173). Bulletin of the Earthquake Research Institute, University of Tokyo.
- Murru, M., Montuori, C., Wyss, M., & Privitera, E. (1999). The locations of magma chambers at Mt. Etna, Italy, mapped by *b*-values. *Geophysical Research Letters*, 26(16), 2553–2556. <https://doi.org/10.1029/1999GL900568>
- Noël, C., Passelègue, F. X., Giorgetti, C., & Violay, M. (2019). Fault reactivation during fluid pressure oscillations: Transition from stable to unstable slip. *Journal of Geophysical Research: Solid Earth*, 124(11), 10940–10953. <https://doi.org/10.1029/2019JB018517>
- Noël, C., Pimienta, L., & Violay, M. (2019). Time-dependent deformations of sandstone during pore fluid pressure oscillations: Implications for natural and induced seismicity. *Journal of Geophysical Research: Solid Earth*, 124(1), 801–821. <https://doi.org/10.1029/2018JB016546>
- Ohnaka, M. (2000). A physical scaling relation between the size of an earthquake and its nucleation zone size. *Pure and Applied Geophysics*, 157(11), 2259–2282. <https://doi.org/10.1007/PL00001084>
- Perfettini, H., Schmittbuhl, J., Rice, J. R., & Cocco, M. (2001). Frictional response induced by time-dependent fluctuations of the normal loading. *Journal of Geophysical Research: Solid Earth*, 106(B7), 13455–13472. <https://doi.org/10.1029/2000JB900366>
- Pétrélis, F., Chanard, K., Schubnel, A., & Hatano, T. (2021). Earthquake sensitivity to tides and seasons: Theoretical studies. *Journal of Statistical Mechanics: Theory and Experiment*, 2021(2), 023404. <https://doi.org/10.1088/1742-5468/abda29>
- Rivière, J., Lv, Z., Johnson, P. A., & Marone, C. (2018). Evolution of *b*-value during the seismic cycle: Insights from laboratory experiments on simulated faults. *Earth and Planetary Science Letters*, 482, 407–413. <https://doi.org/10.1016/j.epsl.2017.11.036>
- Rubinstein, J. L., La Rocca, M., Vidale, J. E., Creager, K. C., & Wech, A. G. (2008). Tidal modulation of nonvolcanic tremor. *Science*, 319(5860), 186–189. <https://doi.org/10.1126/science.1150558>
- Ruina, A. (1983). Slip instability and state variable friction laws. *Journal of Geophysical Research: Solid Earth*, 88(B12), 10359–10370. <https://doi.org/10.1029/JB088iB12p10359>
- Samuelson, J., Elsworth, D., & Marone, C. (2009). Shear-induced dilatancy of fluid-saturated faults: Experiment and theory. *Journal of Geophysical Research: Solid Earth*, 114(B12), B12404. <https://doi.org/10.1029/2008JB006273>
- Savage, H. M., & Marone, C. (2007). Effects of shear velocity oscillations on stick-slip behavior in laboratory experiments. *Journal of Geophysical Research: Solid Earth*, 112(B2), B02301. <https://doi.org/10.1029/2005jb004238>
- Savage, H. M., & Marone, C. (2008). Potential for earthquake triggering from transient deformations. *Journal of Geophysical Research: Solid Earth*, 113(B5), B05302. <https://doi.org/10.1029/2007jb005277>
- Scholz, C. H. (1968). The frequency-magnitude relation of microfracturing in rock and its relation to earthquakes. *Bulletin of the Seismological Society of America*, 58(1), 399–415. <https://doi.org/10.1785/bssa0580010399>
- Scholz, C. H. (2015). On the stress dependence of the earthquake *b*-value. *Geophysical Research Letters*, 42(5), 1399–1402. <https://doi.org/10.1002/2014GL062863>
- Scholz, C. H., Tan, Y. J., & Albino, F. (2019). The mechanism of tidal triggering of earthquakes at mid-ocean ridges. *Nature Communications*, 10(1), 2526. <https://doi.org/10.1038/s41467-019-10605-2>
- Schubnel, A., Fortin, J., Burlini, L., & Gueguen, Y. (2005). Damage and recovery of calcite rocks deformed in the cataclastic regime. *Geological Society, London, Special Publications*, 245(1), 203–221. <https://doi.org/10.1144/gsl.sp.2005.245.01.10>

- Schuster, A. (1897). On lunar and solar periodicities of earthquakes. *Proceedings of the Royal Society of London*, 61(369–377), 455–465. <https://doi.org/10.1038/056321a0>
- Skarbek, R. M., & Savage, H. M. (2019). RSFit3000: A MATLAB GUI-based program for determining rate and state frictional parameters from experimental data. *Geosphere*, 15(5), 1665–1676. <https://doi.org/10.1130/GES02122.1>
- Tan, Y. J., Waldhauser, F., Tolstoy, M., & Wilcock, W. S. D. (2019). Axial Seamount: Periodic tidal loading reveals stress dependence of the earthquake size distribution (*b*-value). *Earth and Planetary Science Letters*, 512, 39–45. <https://doi.org/10.1016/j.epsl.2019.01.047>
- Tanaka, S. (2010). Tidal triggering of earthquakes precursory to the recent Sumatra megathrust earthquakes of 26 December 2004 (Mw 9.0), 28 March 2005 (Mw 8.6), and 12 September 2007 (Mw 8.5). *Geophysical Research Letters*, 37(2). <https://doi.org/10.1029/2009gl041581>
- Tanaka, S. (2012). Tidal triggering of earthquakes prior to the 2011 Tohoku-Oki earthquake (Mw 9.1). *Geophysical Research Letters*, 39(7). <https://doi.org/10.1029/2012GL051179>
- Tolstoy, M., Vernon, F. L., Orcutt, J. A., & Wyatt, F. K. (2002). Breathing of the seafloor: Tidal correlations of seismicity at axial volcano. *Geology*, 30(6), 503–506. [https://doi.org/10.1130/0091-7613\(2002\)030<0503:botstc>2.0.co;2](https://doi.org/10.1130/0091-7613(2002)030<0503:botstc>2.0.co;2)
- Trnkoczy, A. (2009). Understanding and parameter setting of STA/LTA trigger algorithm. In *New Manual of Seismological Observatory Practice (NMSOP)*.
- Wang, W., & Shearer, P. M. (2015). No clear evidence for localized tidal periodicities in earthquakes in the central Japan region. *Journal of Geophysical Research: Solid Earth*, 120(9), 6317–6328. <https://doi.org/10.1002/2015JB011937>
- Wang, W., Shearer, P. M., Vidale, J. E., Xu, X., Trugman, D. T., & Fialko, Y. (2022). Tidal modulation of seismicity at the Coso geothermal field. *Earth and Planetary Science Letters*, 579, 117335. <https://doi.org/10.1016/j.epsl.2021.117335>
- Zhan, Z., & Shearer, P. M. (2015). Possible seasonality in large deep-focus earthquakes. *Geophysical Research Letters*, 42(18), 7366–7373. <https://doi.org/10.1002/2015gl065088>